

# Neural Étendue Expander for Ultra-Wide-Angle High-Fidelity Holographic Display

Ethan Tseng<sup>1</sup>, Seung-Hwan Baek<sup>1,4</sup>, Grace Kuo<sup>2</sup>, Nathan Matsuda<sup>2</sup>, Andrew Maimone<sup>2</sup>, Florian Schiffrers<sup>2</sup>, Praneeth Chakravarthula<sup>1</sup>, Qiang Fu<sup>3</sup>, Wolfgang Heidrich<sup>3</sup>, Douglas Lanman<sup>2</sup>, and Felix Heide<sup>1†</sup>

<sup>1</sup>*Princeton University*

<sup>2</sup>*Reality Labs Research, Meta*

<sup>3</sup>*King Abdullah University of Science and Technology (KAUST)*

<sup>4</sup>*Pohang University of Science and Technology (POSTECH)*

†*Corresponding author. E-mail: fheide@princeton.edu*

**Holographic displays can generate light fields by dynamically modulating the wavefront of a coherent beam of light using a spatial light modulator, promising rich virtual and augmented reality applications. However, the limited spatial resolution of existing dynamic spatial light modulators imposes a tight bound on the diffraction angle. As a result, modern holographic displays possess low étendue, which is the product of the display area and the maximum solid angle of diffracted light. The low étendue forces a sacrifice of either the field-of-view (FOV) or the display size. In this work, we lift this limitation by presenting neural étendue expanders. This new breed of optical elements, which is learned from a natural image dataset, enables higher diffraction angles for ultra-wide FOV while maintaining both a compact form factor and the fidelity of displayed contents to human viewers. With neural étendue expanders, we experimentally achieve  $64\times$  étendue expansion of natural images in full color, expanding the FOV by an order of magnitude horizontally and vertically, with high-fidelity reconstruction quality (measured in PSNR) over 29 dB on retinal-resolution images.**

Holography is the science of creating vivid scenery through carefully crafted interference patterns. This discipline has applications across domains, especially in virtual and augmented reality devices<sup>1,2</sup>. While static holograms can be generated with a suitable recording medium, modern holographic displays typically employ spatial light modulators (SLM) that dynamically modulate the wavefront of a coherent beam<sup>3,4</sup>. However, despite being the workhorse of holography, SLMs suffer from small diffraction angles caused by limitations of modern liquid crystal on silicon (LCoS) technology. Achieving dynamic control with LCoS induces several engineering challenges (e.g., display bandwidth, pixel cross-talk, power consumption), which have imposed a practical lower bound on the pixel pitch<sup>5</sup>. Consequently, the étendue of holographic displays, which is the product of the field-of-view (FOV) and the display size, is fundamentally limited when maintaining a compact SLM size<sup>6</sup>. Holographic displays have to trade off FOV for display size, or vice versa, although both are critical for most display applications. For immersive virtual/augmented reality (VR/AR) devices, an FOV of at least  $120^\circ$  and an eyebox size greater than  $10 \times 10 \text{ mm}^2$  is desired<sup>7</sup>, where the eyebox or display size is defined as the region within which the eye must reside within to view a hologram. To reach the étendue needed for these specific-

ations requires over one billion SLM pixels, which is two orders of magnitude more than what today’s LCoS technology achieves<sup>7</sup>. Manufacturing such a display and dynamically controlling it is beyond modern fabrication and computational capabilities.

Several methods have been proposed to circumvent this problem, including dynamic feedback in the form of eye tracking<sup>8</sup>, spatial integration with multiple SLMs<sup>9</sup>, and temporal integration with laser arrays<sup>10</sup> or fast switching digital micromirror devices<sup>11,12</sup>. However, these approaches require additional dynamic components resulting in high complexity, large form factors, precise timing constraints, and incur additional power consumption. Timing is especially critical for eye tracking solutions as poor latency can result in motion sickness<sup>13</sup>. Rewritable photopolymers are promising alternatives to SLMs for holographic displays, however, they are limited by low refresh rates<sup>14,15</sup>. Microelectromechanical systems have low pixel counts and bit depth<sup>16</sup>. Researchers have also proposed to make trade-offs within the limited étendue of existing holographic displays, such as trading spatial resolution for depth resolution<sup>3</sup> and optimizing for coherent versus incoherent interference<sup>17</sup>, but these methods do not change the total étendue of the display.

Instead, researchers have explored expanding the display étendue by employing optical elements with randomized scattering properties in front of an SLM<sup>7,18–22</sup>. The static nature of these elements facilitates fabrication of pixel areas at the micron-scale, an order of magnitude lower than for a dynamic element such as the SLM, thus resulting in an enlarged diffraction angle<sup>23</sup>. However, existing elements of this type exhibit randomized scattering that is agnostic to the optical setup and the images to be displayed. As modern SLMs have limited degrees of freedom for wavefront shaping, the random modulation delivered by these scattering elements results in low-fidelity étendue expanded holograms. Relaxing high frequencies beyond the human retinal resolution improves the fidelity, however the displayed holograms still suffer from low reconstruction fidelity<sup>7</sup>. Furthermore, extensive calibration is necessary in the case where the scattering properties are unknown<sup>22,24–27</sup>. Recent work explores using lenses and lenslet arrays<sup>28</sup> to expand the field-of-view but this approach forces the eye pupil’s position to match that of the lenses or lenslets, thus shrinking the effective eyebox size, see Supplementary Note 5 for comparison experiments. Another line of work investigates tilting cascades<sup>29</sup>, however, this system has a large physical footprint consisting of several 4F relays. Specifically, this system requires one 4F relay per  $2\times$  factor of étendue expansion, thus three 4F relays are needed to achieve  $8\times$  expansion along one axis, spanning roughly a meter in length. Moreover, the approach requires two parallel cascades to expand the étendue in both the horizontal and vertical directions, further increasing the physical form factor.

In this work, we lift these limitations with neural étendue expanders, a new breed of static optical elements that have been optimized for étendue expansion and accurate reproduction of natural images when combined with an SLM (Fig. 1). These optical elements inherit the aforementioned benefits of scattering elements. However, unlike existing random scattering masks, neural étendue expanders are jointly learned together with the SLM pattern across a natural image dataset. We devise a differentiable holographic image formation model that enables learning via first-order

stochastic optimization. The resulting learned wavefront modulation pushes reconstruction noise outside of the perceivable frequency bands of human visual systems while retaining perceptually critical frequency bands of natural images. We provide analysis that validates that the learned optical elements possess these properties. In simulation, we demonstrate étendue-expanded holograms at  $64\times$  étendue expansion factor with perceptual display quality over 29 dB peak signal-to-noise ratio (PSNR), more than one order of magnitude in reduced error over the existing methods. Furthermore, the expanders also facilitate high-fidelity étendue expanded 3D color holograms of natural scenes, see Supplementary Information, and the elements are also robust to varying pupil positions within the eyebox. We experimentally validate the method with a 1K-pixel SLM to expand the FOV by  $8\times$  in each direction. Since the improvement in display quality depends on the étendue expansion factor and not on the native resolution of the SLM, our  $64\times$  neural étendue expander enables high-fidelity ultra-wide-angle holographic projection of natural images when using an 8K-pixel SLM<sup>30</sup>. Notably, an 8K-pixel SLM combined with  $64\times$  étendue expansion can cover 85% of the human stereo FOV<sup>31</sup> with an 18.5 mm eyebox size, providing a high-fidelity, immersive VR/AR experience.

## Neural étendue expansion

Holographic displays modulate the wavefront of a coherent light beam using an SLM to form an image at a target location. The étendue of a holographic display<sup>32</sup> is then defined as the product of the SLM display area  $A$  and the solid angle of the diffracted light as

$$G_s = 4A \sin^2 \theta_s, \quad (1)$$

where  $\theta_s = \sin^{-1} \frac{\lambda}{2\Delta_s}$  is the maximum diffraction angle of the SLM,  $\lambda$  is the wavelength of light, and  $\Delta_s$  is the SLM pixel pitch. Most SLMs have large  $\Delta_s$  resulting in small  $\theta_s$  as shown in Fig. 1a. We enlarge the display étendue by placing a neural étendue expander in front of the SLM as a static optical element with pixel pitch  $\Delta_n < \Delta_s$ , see Fig. 1b. The smaller pixel pitch  $\Delta_n$  increases the maximum diffraction angle  $\theta_n$ , resulting in an expanded étendue  $G_n = 4A \sin^2 \theta_n$ .

To generate étendue-expanded high-fidelity holograms, we propose a computational inverse-design method that learns the wavefront modulation of the neural étendue expander by treating it as a layer of trainable neurons that are taught to minimize a loss placed on the formed holographic image, see Fig. 1c. Specifically, we model the holographic image formation in a fully differentiable manner following Fourier optics. We relate the displayed holographic image  $I$  to the wavefront modulation of the neural étendue expander  $\mathcal{E}$  as

$$I = |\mathcal{F}(\mathcal{E} \odot U(\mathcal{S}))|^2, \quad (2)$$

where  $\mathcal{F}$  is the 2D Fourier transform,  $\mathcal{S}$  is the SLM modulation,  $U(\cdot)$  is zeroth-order upsampling operator from the low-resolution SLM to the high-resolution neural étendue expander, and  $\odot$  is the Hadamard product.

The differentiability of Eq. (2) with respect to the modulation variables  $\mathcal{E}$  and  $\mathcal{S}$  allows us to learn the optimal wavefront modulation of the neural étendue expander  $\mathcal{E}$  by jointly optimizing the static neural étendue expander in conjunction with the dynamic SLM modulation patterns  $\mathcal{S}$ . That is, for a given image, we optimize the optimal SLM pattern similar to conventional computer-generated holography<sup>33–35</sup>, however, we also simultaneously optimize the neural étendue expander. The SLM and the neural étendue expander cooperate to generate an étendue-expanded high-fidelity hologram. We formulate this joint optimization as

$$\underset{\mathcal{E}, \mathcal{S}_{\{1, \dots, K\}}}{\text{minimize}} \sum_{k=1}^K \left\| \left( |\mathcal{F}(\mathcal{E} \odot U(\mathcal{S}_k))|^2 - T_k \right) * f \right\|_2^2, \quad (3)$$

where  $\mathcal{S}_k$  is the SLM wavefront modulation for the  $k$ -th target image  $T_k$  in a natural-image dataset with  $K$  training samples,  $*$  is the convolution operator, and  $f$  is the low-pass Butterworth filter for approximating the viewer’s retinal resolution as a frequency-cutoff function<sup>7</sup> as

$$f = \mathcal{F}^{-1} \left( \left( 1 + \left( \frac{\|w\|^2}{c^2} \right)^5 \right)^{-1} \right), \quad (4)$$

where  $\mathcal{F}^{-1}$  is the inverse 2D Fourier transform,  $w$  is the spatial frequency, and  $c$  is the cutoff frequency. In order to set the cutoff frequency to be beyond human perceptibility, it suffices to set  $c$  to be  $\frac{\Delta_n N}{\sqrt{\pi}}$  where  $N$  is the SLM pixel count. This is because an 8K-pixel SLM<sup>30</sup> can provide an angular resolution of 61 pixels/degree at an eyebox size of 18.5 mm, see Supplementary Note 3 for details, whereas the angular resolution of the human eye is limited to 60 pixels/degree<sup>7</sup>.

The optimization objective in Eq. (3) jointly optimizes a single static element  $\mathcal{E}$  and a set of SLM patterns  $\mathcal{S}_{\{1, \dots, K\}}$  so that the set of generated holograms matches the target set of natural images  $T_{\{1, \dots, K\}}$ . This objective function is fully differentiable with respect to the wavefront modulations of the SLM and the neural étendue expander. As such, we can solve this optimization problem by training the neural étendue expander and the SLM states akin to a shallow neural network by using stochastic gradient solvers<sup>36</sup>. Our computational design approach is data-driven and requires a dataset of natural images. We used 105 high-resolution training images of natural scenes. For testing, we used 20 natural images. We use grayscale images when designing neural étendue expanders for a monochromatic display, while the original RGB images are used when designing for a trichromatic display.

## Neural étendue expanded holographic display

We validate neural étendue expansion experimentally with a holographic display prototype. See Fig. 2a for a schematic of the hardware prototype and Supplementary Notes 9 and 10 for further details on the experimental setup. We fabricate neural étendue expanders with a pitch of  $2 \mu\text{m}$  with resin stamping, see Supplementary Note 8 for fabrication details. The fabricated expanders are



then placed at the conjugate plane of the SLM to establish pixel-wise correspondence between the SLM and the expander. A DC block is further employed to filter out the undiffracted light from the SLM. To assess the proposed elements, we also compare to fabricated binary random expanders<sup>7</sup> designed for 660 nm. Microscope images of both expanders are shown in Fig. 2b. We acquire holograms corresponding to conventional non-étendue expanded holography<sup>1</sup>,  $64\times$  étendue expanded full color holograms produced with the binary random expanders, and  $64\times$  étendue expanded full color holograms produced with the neural étendue expanders. The illumination wavelengths are 450 nm, 520 nm, and 660 nm. We report captures in Fig. 2c and provide additional measurements in Supplementary Video 1 and in Supplementary Note 1. The captured holograms are tone-mapped for visualization. For fair comparison we applied the same tone-mapping scheme to all holograms, see Supplementary Note 1 for details.

The experimental findings on the display prototype verify that conventional non-étendue expanded holography can produce high-fidelity content but at the cost of a small FOV. Increasing the étendue via a binary random expander will increase the FOV but at the cost of low image fidelity, even at the design wavelength of 660 nm, and chromatic artifacts. The étendue expanded holograms produced with the neural étendue expanders are the only holograms that showcase both ultra-wide-FOV and high-fidelity. The captured holograms demonstrate high contrast and are free from chromatic aberrations. Fig. 2d reports the étendue expanded hologram produced with both expanders at each color wavelength. Since the binary random expander is, by design, only tailored to a single wavelength, in this case 660 nm, the étendue expanded holograms that are generated with it exhibit severe chromatic artifacts. In contrast, holograms generated with neural étendue expansion show consistent high-fidelity performance at all illumination wavelengths. Notably, even at the wavelength of 660 nm the hologram fidelity is higher for the holograms generated with neural étendue expansion, see Fig. 2c. For comparisons against a uniform random expander, where the phase profile is uniformly randomly selected from within  $[0, 2\pi]$ , see Fig. 3 and Supplementary Note 2.

While our experimental prototype was built for a HOLOEYE-PLUTO which possesses a 1K-pixel resolution, corresponding to a 1 mm eyebox with  $75.6^\circ$  horizontal and vertical FOV, the improvement in hologram fidelity persists across resolutions. Irrespective of the resolution of the SLM, performing  $4\times$ ,  $16\times$ , or  $64\times$  étendue expansion with neural étendue expanders results in a similar margin of improvement over uniform and binary random expanders. This is because the improvement in fidelity depends only on the étendue expansion factor. To validate this we simulate an 8K-pixel SLM with  $64\times$  étendue expansion and we verify that the improvement in fidelity is maintained. See Supplementary Note 6 for results and further details. Thus, neural étendue expansion enables high fidelity expansion for  $64\times$  étendue expansion for 8K-pixel SLMs<sup>30</sup>, providing étendue to cover 85% of the human stereo FOV<sup>31</sup> with a 18.5 mm eyebox size, see Supplementary Note 3 for details.

## Characterization of étendue expansion

Next, we analyze the expansion of étendue achieved with the proposed technique. To this end, suppose we want to generate the étendue-expanded hologram of only a single scene. Then, the optimal complex wavefront modulation for the neural étendue expander would be the inverse Fourier transform of the target scene, and, as such, we do not require any additional modulation on the SLM. The SLM therefore can be set to zero-phase modulation. If we generalize this single-image case to diverse natural images, the neural étendue expander is expected to preserve the common frequency statistics of natural images, while the SLM fills in the image-specific residual frequencies to generate a specific target image. In contrast, existing random scatters used for étendue expansion do not consider any natural-image statistics<sup>7, 18, 20, 21</sup>.

To assess whether the optimized neural étendue expander  $\mathcal{E}$ , shown in Fig. 1b, has learned the image statistics of the training set we evaluate the virtual frequency modulation  $\tilde{\mathcal{E}}$ , defined as the spectrum of the generated image with the neural étendue expander and the zero-phase SLM modulation as

$$\tilde{\mathcal{E}} = \mathcal{F}(|\mathcal{F}(\mathcal{E})|^2). \quad (5)$$

The findings in Fig. 1d confirm that the magnitude of the virtual frequency modulation  $|\tilde{\mathcal{E}}|$  resembles the magnitude spectrum of natural images within the passband. Moreover, we observe that the virtual frequency modulation pushes undesirable energy outside of the passband of the human retina as imperceptible high-frequency noise.

To further understand this property of a neural étendue expander, we consider the reconstruction loss  $\mathcal{L}_T$  for a specific target image  $T$ . Using the zero-phase setting for the SLM as an initial point for the first-order stochastic optimization and applying Parseval’s theorem places an upper bound on the reconstruction loss

$$\mathcal{L}_T = \min_S \|(|\mathcal{F}(\mathcal{E} \odot U(S))|^2 - T) * f\|_2^2 \leq \frac{1}{N} \left\| \left( \tilde{\mathcal{E}} - \mathcal{F}(T) \right) \odot \mathcal{F}(f) \right\|_2^2, \quad (6)$$

where  $N$  is the pixel count of the neural étendue expander. Please see Supplementary Note 3 for further details of how this upper bound is found. Therefore, obtaining the optimal neural étendue expander, which minimizes the reconstruction loss  $\mathcal{L}_T$ , results in the virtual frequency modulation  $\tilde{\mathcal{E}}$  that resembles the natural-image spectrum  $\mathcal{F}(T)$  averaged over diverse natural images. Also, the retinal frequency filter  $\mathcal{F}(f)$  leaves the higher spectral bands outside of the human retinal resolution unconstrained. This allows the neural étendue expander to push undesirable energy towards higher frequency bands, which then manifests as imperceptible high-frequency noise to human viewers.

We investigate the image statistics preserved by the neural étendue expanders by visualizing  $|\tilde{\mathcal{E}}|$ . Fig. 3e visualizes the learned expander pattern  $\mathcal{E}$  for increasing étendue expansion factors, specifically for  $4\times$ ,  $16\times$ ,  $36\times$ , and  $64\times$  expansion. Unlike uniform and binary random expanders,

the learned expanders exhibit high and low frequency structures. Fig. 3f shows the corresponding virtual frequency  $|\tilde{\mathcal{E}}|$  for each étendue expansion factor. We observe that the interwoven high and low frequency patterns on each learned expander correspond to a virtual frequency that pushes noise outside of the retinal frequency bands defined by  $\mathcal{F}(f)$ . Furthermore, the frequency structure within the passband resembles the frequency structure of the natural image training dataset, see Fig. 3c.

To characterize the hologram reconstruction with the proposed neural étendue expander we simulate a Fourier holographic setup that has been augmented with a neural étendue expander. Fig. 3a reports qualitative examples of trichromatic and monochromatic reconstructions achieved with neural étendue expanders, binary random expanders<sup>7</sup>, photon sieves<sup>21</sup>, and conventional holography<sup>1</sup>. See Supplementary Note 2 for additional qualitative comparisons and for comparisons against uniform random expanders. The uniform random expander is constructed by assigning each pixel a phase that is uniformly randomly chosen within  $[0, 2\pi]$ . To ensure at least  $2\pi$  phase is available for all wavelengths the  $[0, 2\pi]$  phase range is defined for 660 nm. Conventional holography is subject to a low display étendue that is limited by the SLM native resolution, thus resulting in a low FOV. Photon sieves, binary random expanders, and uniform random expanders have low reconstruction fidelity, resulting in severe noise and low contrast in the generated holograms. In the case of the trichromatic holograms, both uniform and binary random expanders do not facilitate consistent étendue expansion at all wavelengths, which results in chromatic artifacts. Although the uniform random expander provides at least  $2\pi$  phase coverage for all wavelengths, the variation in refractive index across wavelengths results in differing phase profiles. Thus, although the uniform random expander has the same degree of quantization as neural étendue expanders, it does not enable étendue expanded trichromatic holograms. Photon sieves scatter light equally across wavelengths but their randomized amplitude-only modulation does not allow for high-fidelity reconstruction of natural images, see Fig. 3d for quantitative metrics and Supplementary Note 2 for qualitative examples and additional metrics. Neural étendue expansion is the only technique that facilitates high-fidelity reconstructions for both trichromatic and monochromatic setups. We quantitatively verify this by evaluating the reconstruction fidelity on an unseen test dataset, where fidelity is measured in peak signal-to-noise ratio (PSNR). Fig. 3b shows that neural étendue expanders achieve over 14 dB PSNR improvement favorable to other expanders when generating  $64\times$  étendue expanded trichromatic holograms. For monochromatic holograms, neural étendue expansion achieves over 10 dB PSNR improvement. Thus, neural étendue expansion allows for an order of magnitude improvement over existing étendue expansion methods. See Fig. 3d for quantitative evaluations at different étendue expansion factors. See Supplementary Note 2 for further simulation details and more comparison examples.

In addition to field-of-view, we also investigate the eyebox that is produced with neural étendue expansion. By initializing the learning process with a uniform random expander we bias the optimized solution towards expanders that distribute energy throughout the eyebox, in contrast to a quadratic phase profiles<sup>28</sup> that concentrate the energy at fixed points. Thus, the viewer’s eye pupil can freely move within the eyebox and observe the wide field-of-view hologram at any loc-

ation. We incorporate pupil-aware optimization<sup>37</sup> to preserve the perceived hologram quality at different eye pupil locations. See Supplementary Note 5 for findings. Finally, we also investigate 3D étendue expanded holograms. We find that neural étendue expansion also enables higher fidelity étendue expanded 3D color holograms. We note that existing methods on étendue expanded holography has focused on monochromatic 3D holograms<sup>7,28,29</sup>. Photon sieves<sup>21</sup> only achieves 3D color holography for sparse points. See Supplementary Note 4 for a discussion of these findings.

## Discussion

In this work, we introduce neural étendue expanders as an optical element that expands the étendue of existing holographic displays without sacrificing displayed hologram fidelity. Neural étendue expanders are learned from a natural image dataset and are jointly optimized with the SLM’s wavefront modulation. Akin to a shallow neural network, this new breed of optical elements allows us to tailor the wavefront modulation element to the display of natural images and maximize display quality perceivable by the human eye. As the first learned optics for étendue expansion, we achieve étendue expansion factor  $64\times$  with over 29 dB PSNR reconstructions, an order of magnitude improvement over existing approaches. This means that expansion factor  $64\times$  combined with an 8K-pixel SLM can enable high-fidelity, ultra-wide-angle holographic projection of natural images with  $126^\circ$  FOV and 18.5 mm eyebox size, covering more than 85% of the human FOV. Furthermore, neural étendue expanders support multi-wavelength illumination for color holograms. The expanders also support 3D color holography and viewer pupil-awareness. We envision that future holographic displays may incorporate the described optical design approach into their construction, especially for VR/AR displays. Extending our work to utilize other types of emerging optics such as metasurfaces may prove to be a promising direction for future work, as diffraction angles can be greatly enlarged by nano-scale metasurface features<sup>38</sup> and additional properties of light such as polarization can be modulated using meta-optics<sup>39</sup>.

## Methods

**Simulation** We used PyTorch to design and evaluate the neural étendue expanders. See Supplementary Notes 2 and 3 for details on the optimization framework, evaluation, and analysis.

**Fabrication** The expanders are physically realized as diffractive optical elements (DOE). Fabricating the DOEs consists of several stages. The first stage consists of etching the negative of the desired pattern onto a substrate. This etching is performed with laser beam lithography. The etched substrate forms a stamp which is then pressed onto a resin mold that is mounted on a glass substrate. The resin itself contains the final pattern. The resin has a wavelength dependent refractive index that we incorporate into our design framework. For the resin we used, the refractive indices are 1.5081 for 660 nm, 1.5159 for 517 nm, and 1.5223 for 450 nm. See Supplementary Note 8 for details.

**Experimental Setup** We evaluated the neural étendue expanders using a prototype holographic display. The prototype consists of a HOLOEYE-PLUTO SLM, a 4F system, a DC block, and a camera for imaging the étendue expanded holograms. See Supplementary Notes 9 and 10 for details.

**Data Availability** The code and data used to generate the findings of this study will be made public on GitHub.

**Code Availability** The code and data used to generate the findings of this study will be made public on GitHub.

## References

1. Shi, L., Li, B., Kim, C., Kellnhofer, P. & Matusik, W. Towards real-time photorealistic 3d holography with deep neural networks. *Nature* **591**, 234–239 (2021).
2. Itoh, Y., Langlotz, T., Sutton, J. & Plopski, A. Towards indistinguishable augmented reality: A survey on optical see-through head-mounted displays. *ACM Computing Surveys (CSUR)* **54**, 1–36 (2021).
3. Dorrah, A. H. *et al.* Light sheets for continuous-depth holography and three-dimensional volumetric displays. *Nature Photonics* **17**, 427–434 (2023).
4. Wakunami, K. *et al.* Projection-type see-through holographic three-dimensional display. *Nature Communications* **7**, 12954 (2016).
5. Moser, S., Ritsch-Marte, M. & Thalhammer, G. Model-based compensation of pixel crosstalk in liquid crystal spatial light modulators. *Optics Express* **27**, 25046–25063 (2019).
6. Lohmann, A. W., Dorsch, R. G., Mendlovic, D., Zalevsky, Z. & Ferreira, C. Space–bandwidth product of optical signals and systems. *JOSA A* **13**, 470–473 (1996).
7. Kuo, G., Waller, L., Ng, R. & Maimone, A. High resolution étendue expansion for holographic displays. *ACM Transactions on Graphics (TOG)* **39**, 1–14 (2020).
8. Choi, M.-H., Ju, Y.-G. & Park, J.-H. Holographic near-eye display with continuously expanded eyebox using two-dimensional replication and angular spectrum wrapping. *Optics Express* **28**, 533–547 (2020).
9. Hahn, J., Kim, H., Lim, Y., Park, G. & Lee, B. Wide viewing angle dynamic holographic stereogram with a curved array of spatial light modulators. *Optics Express* **16**, 12372–12386 (2008).
10. Lee, B. *et al.* Wide-angle speckleless dmd holographic display using structured illumination with temporal multiplexing. *Optics Letters* **45**, 2148–2151 (2020).

11. Kim, M. *et al.* Expanded exit-pupil holographic head-mounted display with high-speed digital micromirror device. *ETRI Journal* **40** (2018).
12. Hellman, B. & Takashima, Y. Angular and spatial light modulation by single digital micromirror device for multi-image output and nearly-doubled étendue. *Optics express* **27** **15**, 21477–21496 (2019).
13. Wetzstein, G., Heidrich, W. & Luebke, D. Optical image processing using light modulation displays. *Computer Graphics Forum* **29** (2010).
14. Blanche, P.-A. *et al.* Holographic three-dimensional telepresence using large-area photorefractive polymer. *Nature* **468**, 80–83 (2010).
15. Tay, S. *et al.* An updatable holographic three-dimensional display. *Nature* **451**, 694–698 (2008).
16. Ersumo, N. T. *et al.* A micromirror array with annular partitioning for high-speed random-access axial focusing. *Light: Science & Applications* **9**, 1–15 (2020).
17. Yang, D. *et al.* Diffraction-engineered holography: Beyond the depth representation limit of holographic displays. *Nature Communications* **13** (2022).
18. Buckley, E., Cable, A., Lawrence, N. & Wilkinson, T. Viewing angle enhancement for two- and three-dimensional holographic displays with random superresolution phase masks. *Applied Optics* **45**, 7334–7341 (2006).
19. Huang, K. *et al.* Ultrahigh-capacity non-periodic photon sieves operating in visible light. *Nature Communications* **6**, 7059 (2015).
20. Yu, H., Lee, K., Park, J. & Park, Y. Ultrahigh-definition dynamic 3d holographic display by active control of volume speckle fields. *Nature Photonics* **11**, 186–192 (2017).
21. Park, J., Lee, K. & Park, Y. Ultrathin wide-angle large-area digital 3d holographic display using a non-periodic photon sieve. *Nature Communications* **10**, 1304 (2019).
22. Yu, P. *et al.* Ultrahigh-density 3d holographic projection by scattering-assisted dynamic holography. *Optica* **10**, 481–490 (2023).
23. Genet, C. & Ebbesen, T. Light in tiny holes. *Nature* **445**, 39–46 (2007).
24. Mosk, A. P., Lagendijk, A., Leroose, G. & Fink, M. Controlling waves in space and time for imaging and focusing in complex media. *Nature Photonics* **6**, 283–292 (2012).
25. Conkey, D. B. *et al.* Super-resolution photoacoustic imaging through a scattering wall. *Nature Communications* **6**, 7902 (2015).
26. Vellekoop, I. M., Lagendijk, A. & Mosk, A. Exploiting disorder for perfect focusing. *Nature Photonics* **4**, 320–322 (2010).

27. Popoff, S. M. *et al.* Measuring the transmission matrix in optics: an approach to the study and control of light propagation in disordered media. *Physical Review Letters* **104**, 100601 (2010).
28. Monin, S., Sankaranarayanan, A. C. & Levin, A. Analyzing phase masks for wide étendue holographic displays. In *2022 IEEE International Conference on Computational Photography (ICCP)*, 1–12 (2022).
29. Monin, S., Sankaranarayanan, A. C. & Levin, A. Exponentially-wide etendue displays using a tilting cascade. In *2022 IEEE International Conference on Computational Photography (ICCP)*, 1–12 (2022).
30. Sterling, R. Jvc d-ila high resolution, high contrast projectors and applications. In *Proceedings of the 2008 Workshop on Immersive Projection Technologies/Emerging Display Technologies* (2008).
31. Wheelwright, B. *et al.* Field of view: not just a number. In *Digital Optics for Immersive Displays*, vol. 10676, 1 – 7 (International Society for Optics and Photonics, 2018).
32. Chaves, J. *Introduction to nonimaging optics* (2008).
33. Gerchberg, R. W. A practical algorithm for the determination of phase from image and diffraction plane pictures. *Optik* **35**, 237–246 (1972).
34. Georgiou, A., Christmas, J., Collings, N., Moore, J. & Crossland, W. Aspects of hologram calculation for video frames. *Journal of Optics A: Pure and Applied Optics* **10**, 035302 (2008).
35. Chakravarthula, P., Peng, Y., Kollin, J., Fuchs, H. & Heide, F. Wirtinger holography for near-eye displays. *ACM Transactions on Graphics (TOG)* **38**, 1–13 (2019).
36. Kingma, D. & Ba, J. Adam: A method for stochastic optimization. In *International Conference on Learning Representations (ICLR)* (2015).
37. Chakravarthula, P. *et al.* Pupil-aware holography. *ACM Transactions on Graphics (TOG)* **41** (2022).
38. Scheuer, J. & Yifat, Y. Metasurfaces make it practical. *Nature nanotechnology* **10**, 296–298 (2015).
39. Dorrah, A. H., Rubin, N. A., Zaidi, A., Tamagnone, M. & Capasso, F. Metasurface optics for on-demand polarization transformations along the optical path. *Nature Photonics* **15**, 287–296 (2021).

**Acknowledgements** The authors acknowledge the use of Princeton’s Imaging and Analysis Center (IAC), which is partially supported by the Princeton Center for Complex Materials (PCCM), a National Science Foundation (NSF) Materials Research Science and Engineering Center (MRSEC; DMR-2011750). We thank Ilya Chugunov for providing natural image data.

**Author Contributions**

**Competing Interests** The authors declare no competing financial interests.

**Supplementary Information** Supplementary Information accompanies this manuscript as part of the submission files.

**Correspondence** Correspondence should be addressed to F.H.



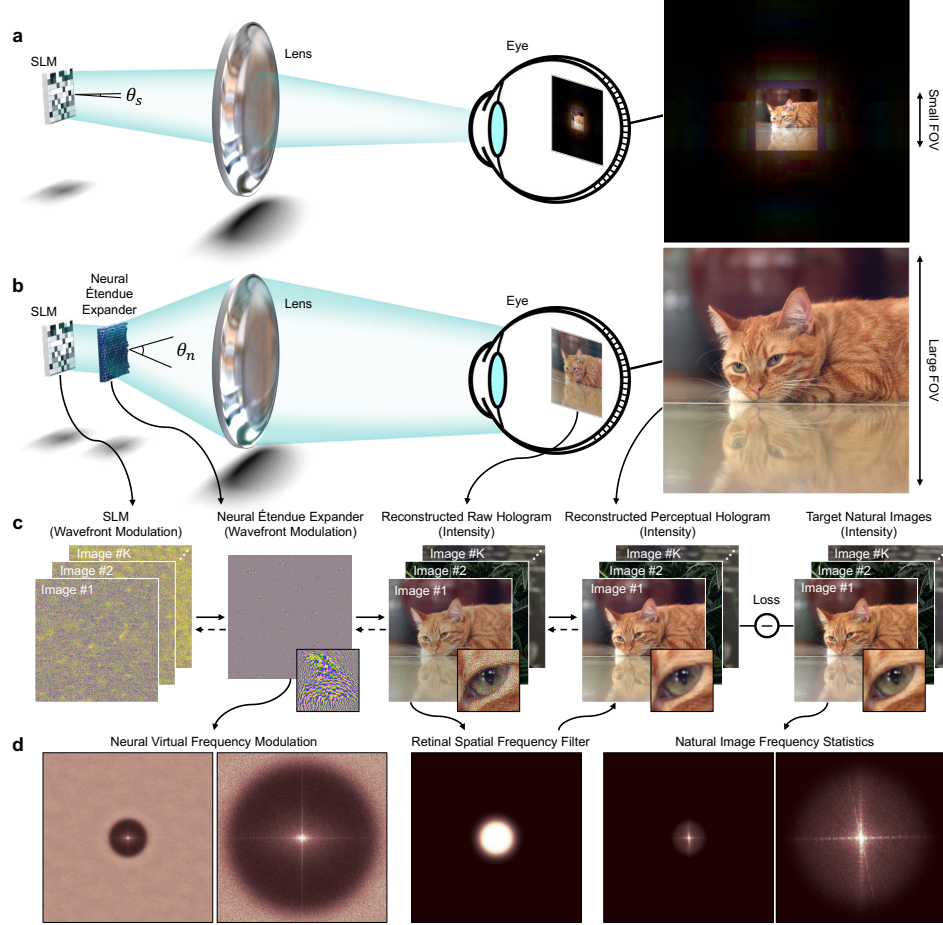


**Figure 1: Neural étendue expansion for ultra-wide angle, high-fidelity holograms.** **a** Conventional holographic displays suffer from low étendue, resulting in either small FOV or eyebox size. Here, we illustrate a small FOV as  $\theta_s$ . **b** Introducing a neural étendue expander into the display facilitates ultra-wide angle holograms, here we illustrate the increase in FOV as  $\theta_n$ . **c** We design the neural étendue expanders via an end-to-end optimization algorithm that considers the SLM wavefront modulation and the human viewer’s perceptual response. One SLM pattern is optimized for each training sample, while the neural étendue expander learns a general structure that facilitates hologram generation of any natural image. **d** The learned neural étendue expander preserves the major frequency bands of natural images within the frequency cutoff determined by the resolution of the human retina.

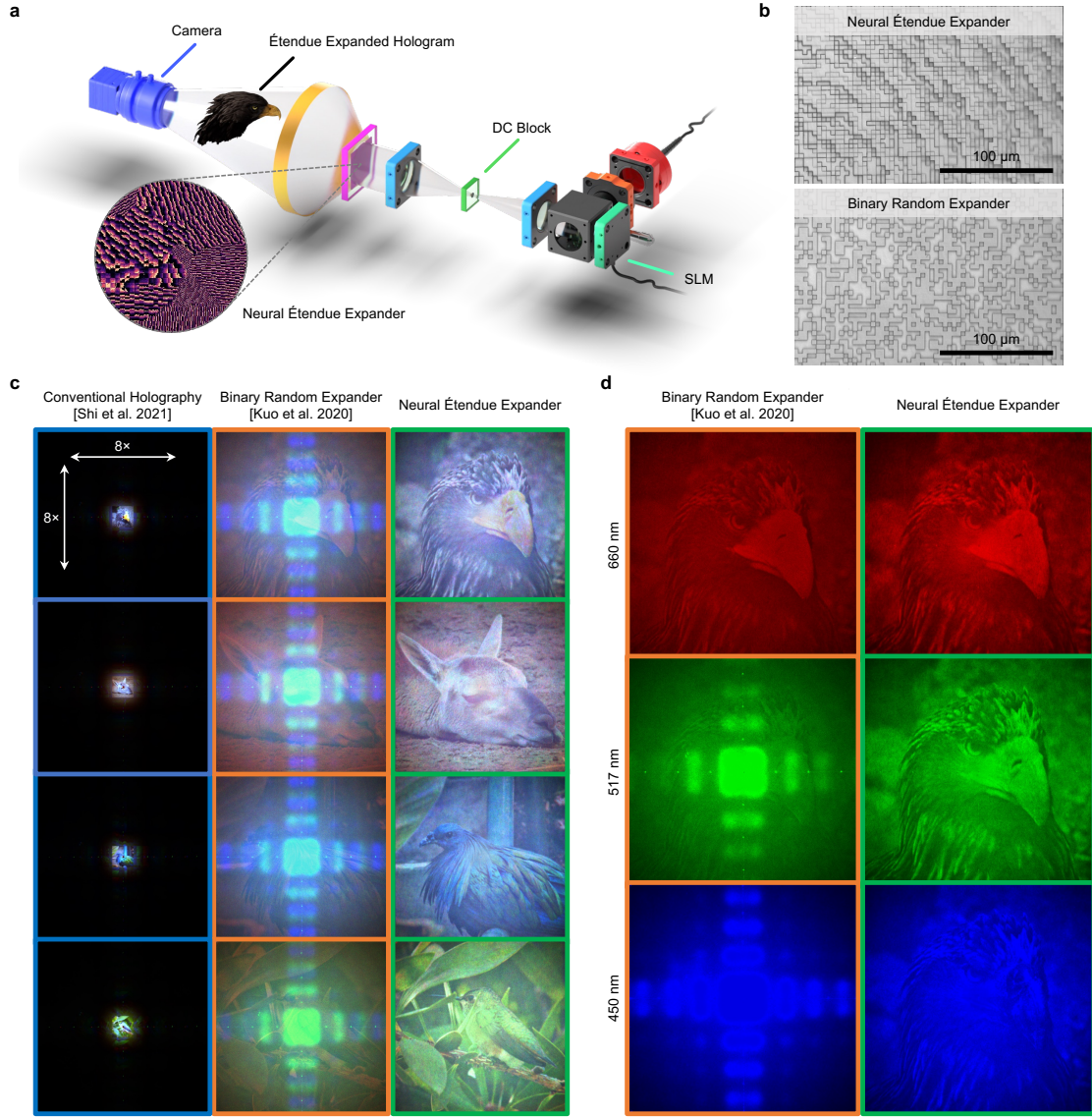


**Figure 2: Experimental demonstration of neural étendue expansion.** **a** Schematic of holographic display prototype with the neural étendue expander inserted at the conjugate plane of the SLM. **b** Microscope images of a fabricated neural étendue expander and a binary random expander<sup>7</sup>. **c** Captures of holograms generated with the display prototype. The small dark circle in the center of the pictures corresponds to the DC block. Left: Non-étendue expanded holograms produced with conventional holography<sup>1</sup>. These holograms have extremely low FOV. Middle:  $64\times$  étendue expanded holograms produced with the binary random expander show low contrast and chromatic artifacts. Right:  $64\times$  étendue expanded holograms produced with the neural étendue expander show high fidelity. **d** Decomposition of  $64\times$  étendue expanded holograms into constituent colors (450 nm, 517 nm, 660 nm). We observe improved hologram contrast and less scatter with neural étendue expansion, even at the wavelength of 660 nm which was used to design the binary random expander.

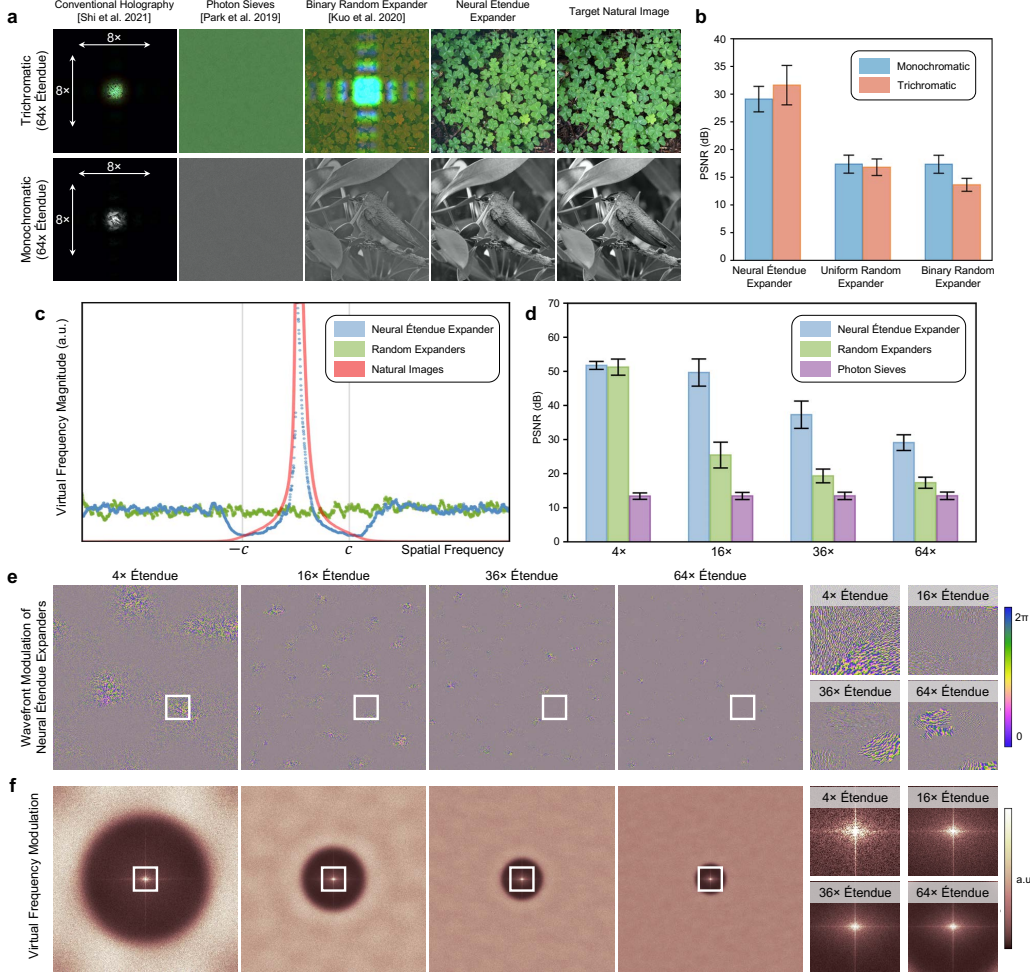


**Figure 3: Étendue expander characterization.** **a** The  $64\times$  étendue expanded holograms generated with neural étendue expanders have the highest fidelity with respect to the target natural image, for both the trichromatic and monochromatic cases. In comparison, the holograms generated with binary random expanders<sup>7</sup> or photon sieves<sup>21</sup> show lower contrast and more speckle noise. Photon sieves could generate étendue expanded holograms of sparse points but not of natural scenes. A low étendue hologram generated with conventional holography<sup>1</sup> and no expander is included for comparison. **b** Quantitative performance comparison of  $64\times$  étendue expanded holograms when using neural, uniform random, and binary random expanders. The metrics are evaluated over an unseen test set. **c** Virtual frequency modulation cross section. Neural étendue expanders push reconstruction artifacts outside of the perceivable frequency bands of human vision while producing a natural image frequency spectrum within the passband as predicted by Eq. 6. In contrast, the both uniform and binary random expanders exhibit a flat spectrum which reduces the reconstruction quality within the passband. The cutoff frequency is indicated by  $c$ . **d** Quantitative reconstruction quality of neural étendue expansion, random expansion, and photon sieves<sup>21</sup> for increasing étendue expansion factors for the monochromatic case. Uniform and binary random expansion both achieve the same performance for a single wavelength. **e** Visualization of the learned expanders for increasing étendue expansion factors. We observe that the learned modulation structures contain both high and low frequency components. **f** Visualization of the corresponding virtual frequency modulation for each expander.

# Neural Étendue Expander for Ultra-Wide-Angle High-Fidelity Holographic Display

## Supplementary Information

Ethan Tseng<sup>1</sup>, Seung-Hwan Baek<sup>1,4</sup>, Grace Kuo<sup>2</sup>, Nathan Matsuda<sup>2</sup>, Andrew Maimone<sup>2</sup>, Florian Schiffrers<sup>2</sup>, Praneeth Chakravarthula<sup>1</sup>, Qiang Fu<sup>3</sup>, Wolfgang Heidrich<sup>3</sup>, Douglas Lanman<sup>2</sup>, and Felix Heide<sup>1†</sup>

<sup>1</sup>*Princeton University*

<sup>2</sup>*Reality Labs Research, Meta*

<sup>3</sup>*King Abdullah University of Science and Technology (KAUST)*

<sup>4</sup>*Pohang University of Science and Technology (POSTECH)*

†*Corresponding author. E-mail: fheide@princeton.edu*

In this document we provide additional discussion and results in support of the primary manuscript.

### Supplementary Video 1: Experimental Assessment for Dynamic Scenes

The Supplementary Videos are experimental video captures of the étendue expanded holograms generated with neural étendue expanders. For comparison, étendue expanded holograms generated with binary random expanders<sup>1</sup> and non-étendue expanded holograms<sup>2</sup> are included. All results shown are captured on the same hardware prototype as described in the manuscript. The results shown in the videos are 2D holograms, see Supplementary Note 4 for 3D hologram results. We use time multiplexing CGH where we compute 3 independent holograms for each frame of each video. The 3 holograms are displayed and captured sequentially and each frame of each video is then computed as the average of the 3 holograms. The refresh rate of the HOLOEYE-PLUTO SLM that we used is 60 Hz, resulting in an effective framerate of 20 Hz after time averaging.

## Supplementary Note 1: Additional Experimental Results

Next, we provide additional experimental findings that were acquired on the experimental setup. Supplementary Fig. S1 reports  $64\times$  étendue expanded color holograms. Supplementary Fig. S2 lists the reconstructions for individual color channels. Supplementary Fig. S3 and Fig. S4 display the corresponding color holograms at  $16\times$  étendue expansion. Supplementary Fig. S5 and Fig. S6 show  $64\times$  and  $16\times$  étendue expanded monochromatic holograms.

We use temporal multiplexing to reduce speckle for all results shown. Specifically, all experimental results shown are computed as the average of 20 holograms, where each hologram is generated with a different random seed. Using a different random seed for each hologram results in different speckle artifacts which are then eliminated through temporal multiplexing.

In addition, we performed white balancing on the captures so that the overall color ratio matches that of the target images. In the future, this color balancing step could have been performed in the hardware via laser power adjustment if we had a programmable laser source.

Lastly, all of the expanders leak a residual DC term similar to how the SLM also leaks a DC term. We suppressed this term by determining the hologram that corresponds to each expander's DC term and then subtracting it from the captured holograms. In the future, the DC term could be eliminated in hardware by using a tilted off-axis construction.



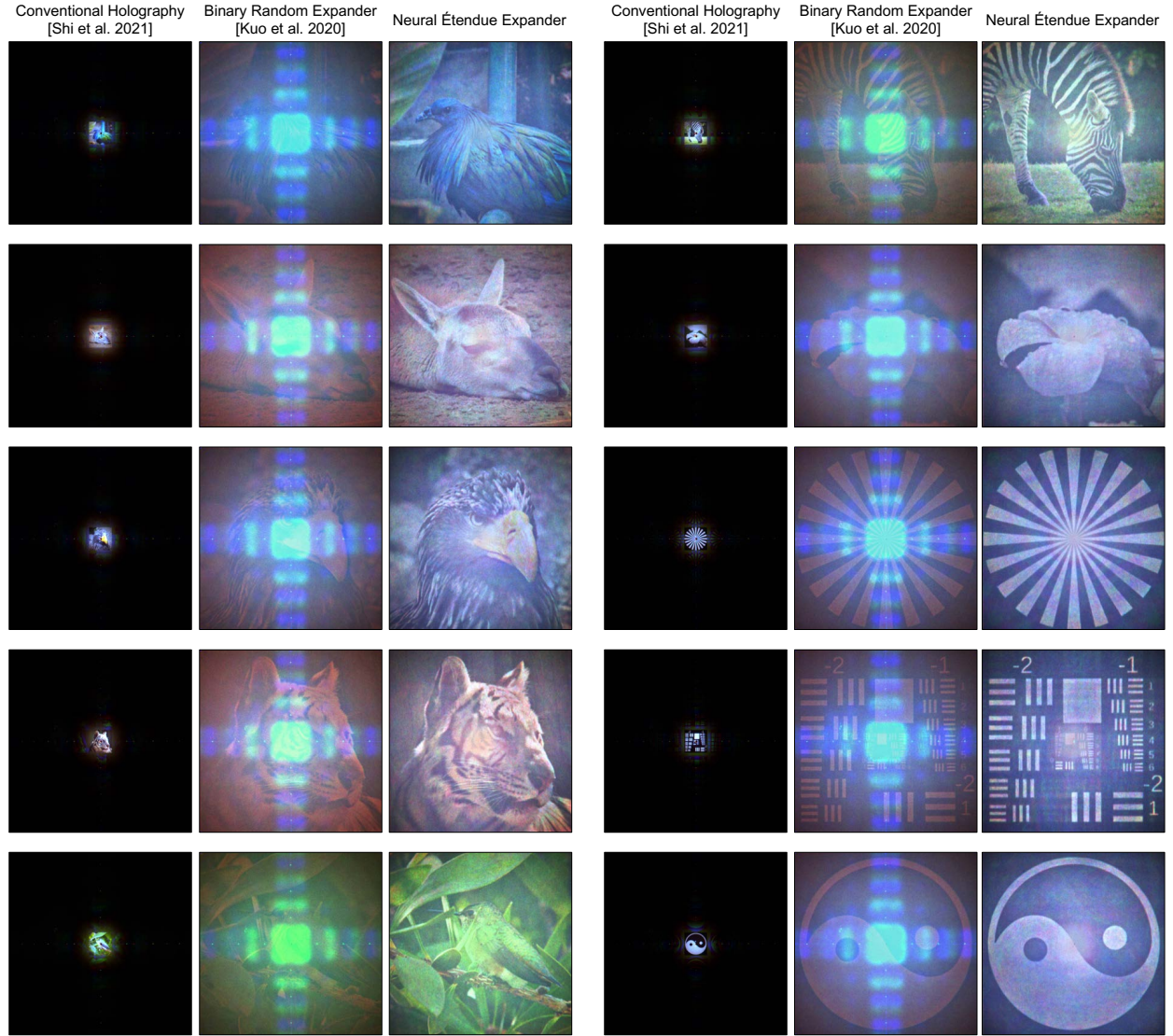


**Figure S1:** Experimentally captured color holograms at  $64\times$  étendue expansion. The wavelengths used are 660 nm, 517 nm, and 450 nm. For comparison, étendue expanded holograms generated with random expanders<sup>1</sup> and non-étendue expanded holograms<sup>2</sup> are included. These results supplement the experimental findings from Fig. 2 of the main manuscript.

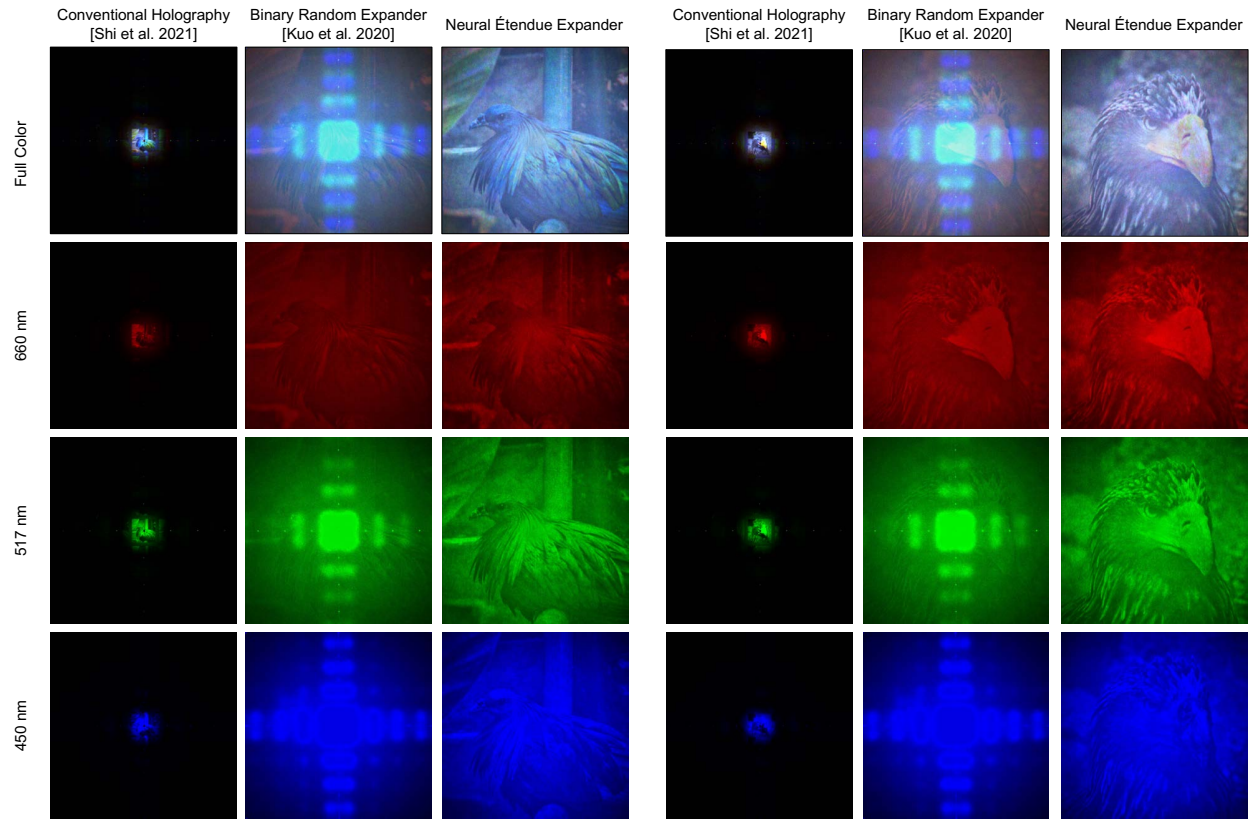


**Figure S2:** Experimentally captured color holograms at  $64\times$  étendue expansion. This figure shows the reconstructions for individual color channels for the holograms shown in Supplementary Fig. S1. These results supplement the experimental findings from Fig. 2 of the main manuscript.

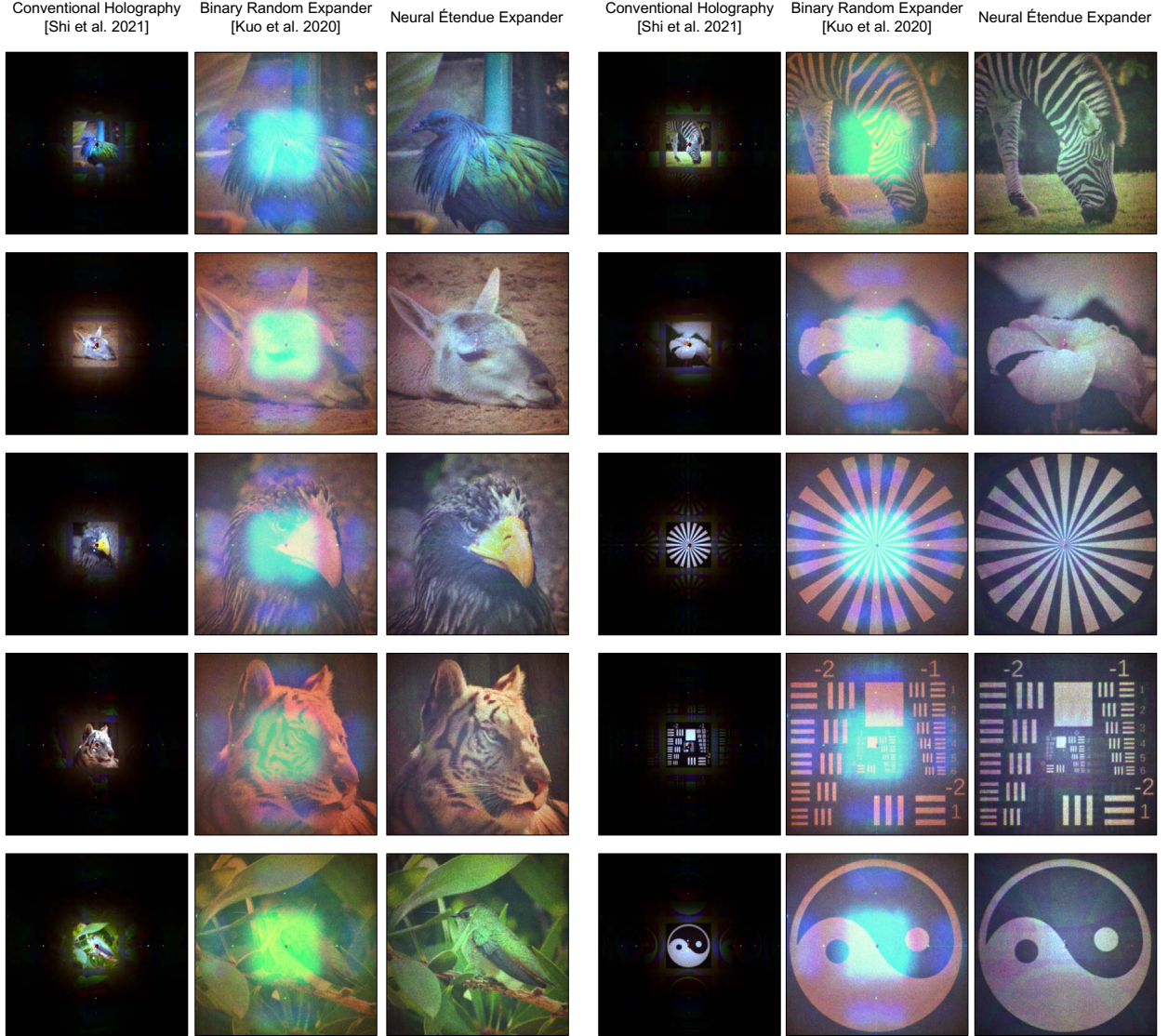


**Figure S3:** Experimentally captured color holograms at  $16\times$  étendue expansion. The wavelengths used are 660 nm, 517 nm, and 450 nm. For comparison, étendue expanded holograms generated with random expanders<sup>1</sup> and non-étendue expanded holograms<sup>2</sup> are included. These results supplement the experimental findings from Fig. 2 of the main manuscript.



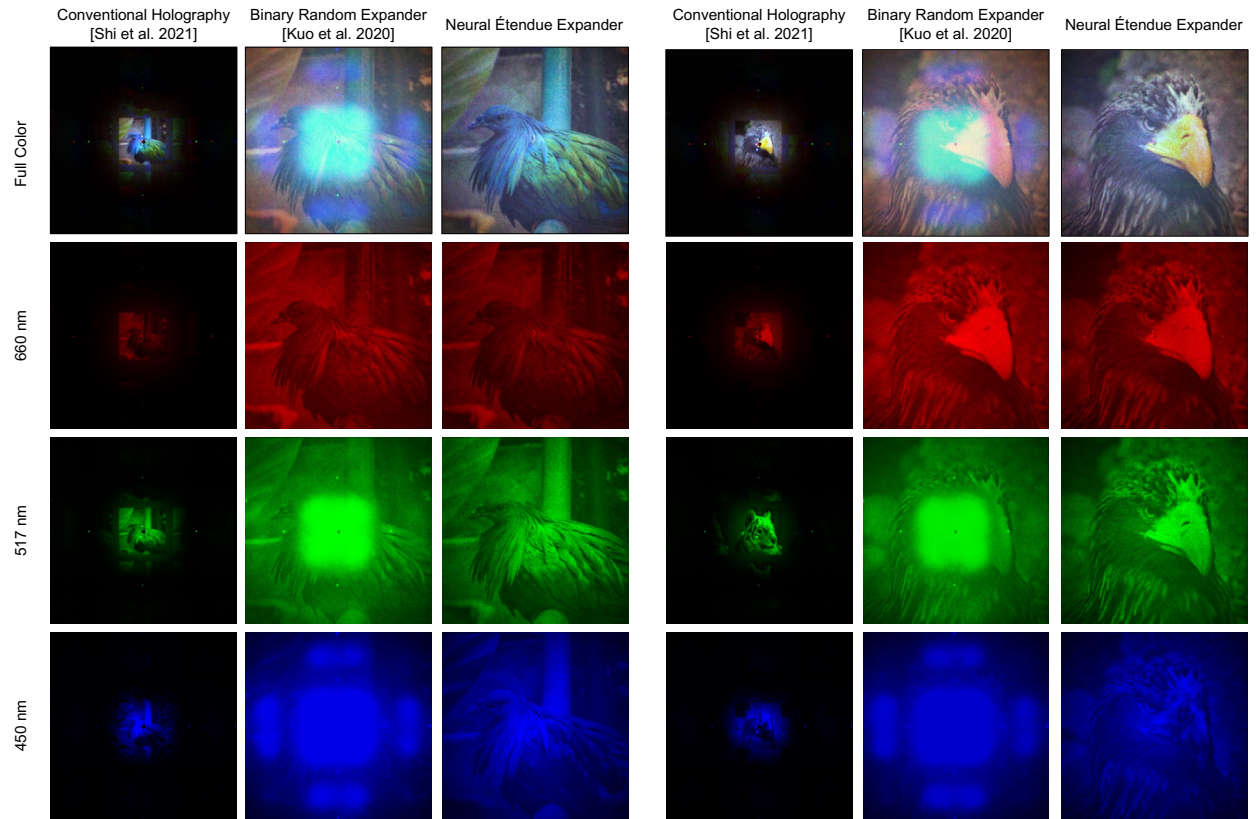


**Figure S4:** Experimentally captured color holograms at  $16\times$  étendue expansion. This figure shows the reconstructions for individual color channels for the holograms shown in Supplementary Fig. S3. These results supplement the experimental findings from Fig. 2 of the main manuscript.

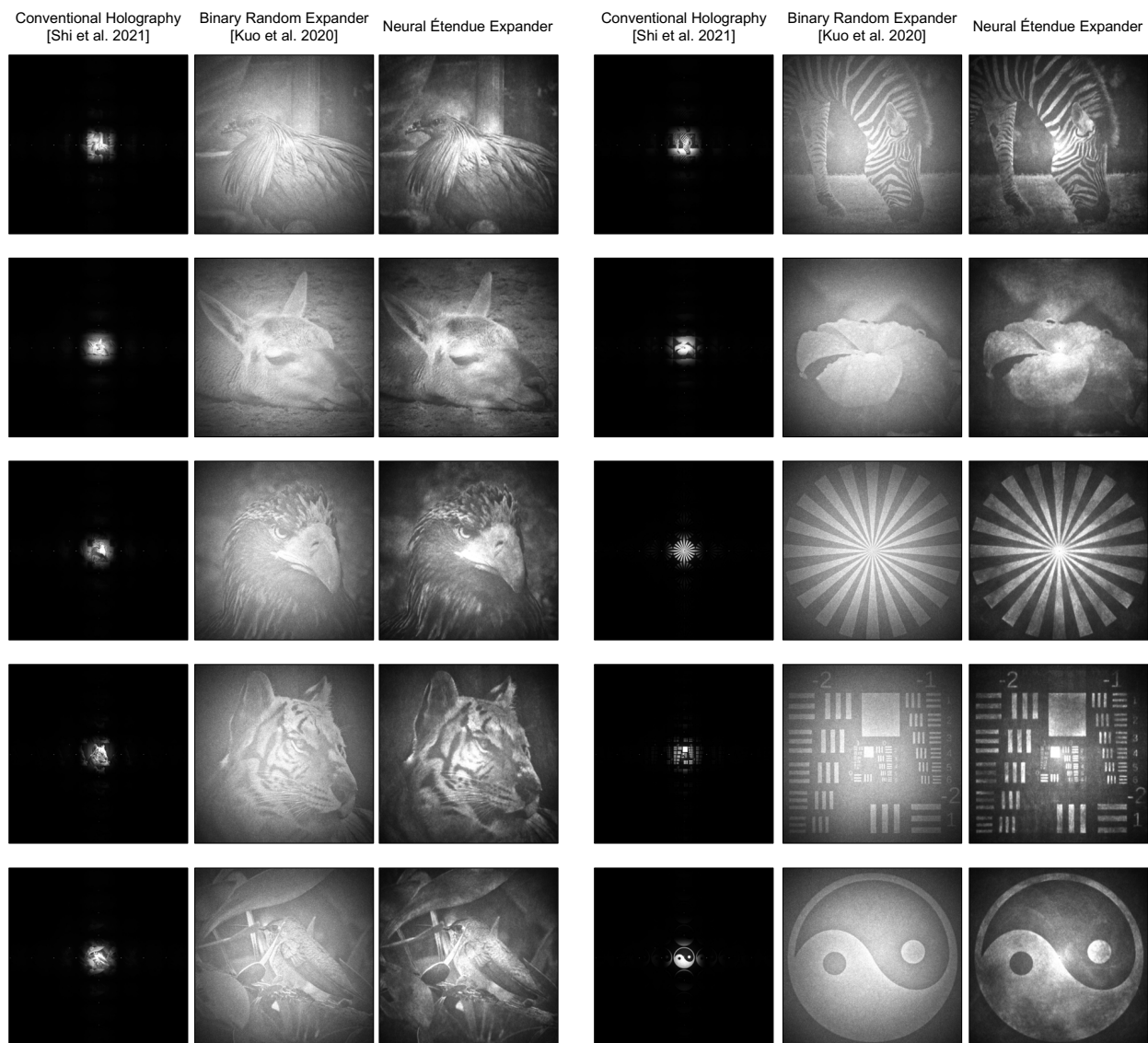


**Figure S5:** Experimentally captured monochromatic holograms at  $64\times$  étendue expansion. The wavelengths used is 660 nm. For comparison, étendue expanded holograms generated with random expanders<sup>1</sup> and non-étendue expanded holograms<sup>2</sup> are included. These results supplement the experimental findings from Fig. 2 of the main manuscript.

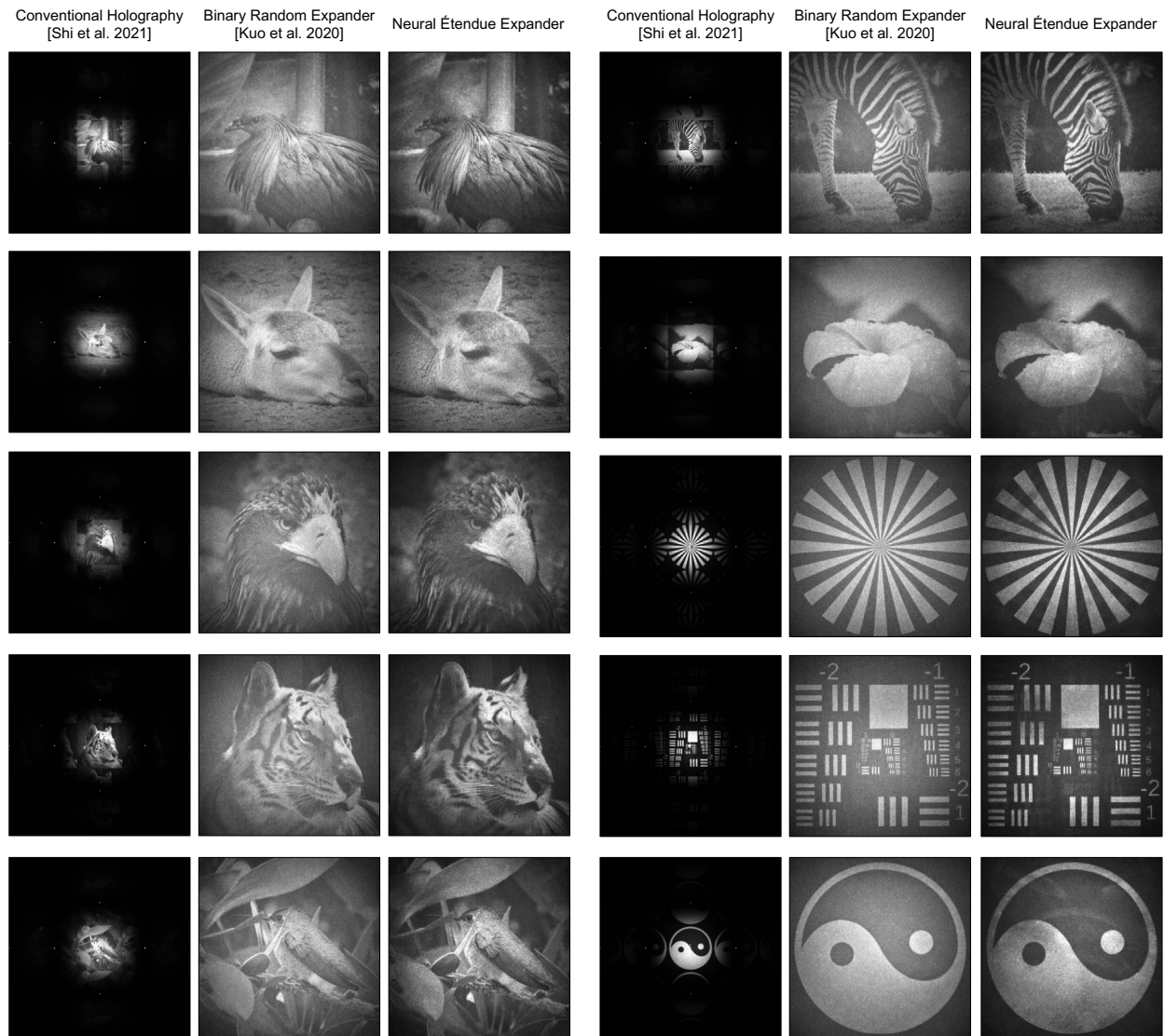


**Figure S6:** Experimentally captured monochromatic holograms at  $16\times$  étendue expansion. The wavelengths used is 660 nm. For comparison, étendue expanded holograms generated with random expanders<sup>1</sup> and non-étendue expanded holograms<sup>2</sup> are included. These results supplement the experimental findings from Fig. 2 of the main manuscript.

## Supplementary Note 2: Additional Synthetic Results

We provide additional simulation results that further validate the effects of neural étendue expansion. Supplementary Fig. S7 compares  $64\times$  étendue expansion with neural étendue expanders against étendue expansion with photon sieves<sup>3</sup> and randomized expanders<sup>1</sup>. Supplementary Fig. S8 reports the same comparison for only a single wavelength. Supplementary Figs. S9 and S10 report the same comparisons for  $16\times$  étendue expansion.

The wavelengths used are the same as in the physical experiment, specifically 660 nm, 517 nm, and 450 nm. The random expanders here are also designed for 660 nm as in the physical experiment. We assume 100% diffraction efficiency for both the SLM and the expander so no DC block is simulated.

Quantitative scores are shown in Supplementary Table S1. The monochromatic evaluation uses a neural étendue expander designed specifically for a single wavelength whereas the trichromatic evaluations use a neural étendue expander designed simultaneously for all three wavelengths. The random expander<sup>1</sup> can only be designed for one wavelength and in this case it is designed for 660 nm. The photon sieve<sup>3</sup> is agnostic to wavelength because it only affects the amplitude component. The training and test datasets consist of images from personal photo collections, the DIV2K dataset<sup>4</sup>, and the INRIA Holiday dataset<sup>5</sup>.

The CGH algorithm used for our method is end-to-end gradient descent optimization with our fully differentiable image formation model<sup>6</sup>. We apply the same CGH algorithm when running baseline comparisons for the random expander. For the photon sieve, we follow the CGH algorithm described in their Supplementary Information. Specifically, we compute a phase-only inverse Fourier transform of the target image using IFTA<sup>7</sup> and then we directly sample the Fourier spectrum at the locations of the holes in the photon sieve.

We incorporate wavelength dependent dispersion into these simulations. As such, the full color holograms are generated by slightly reducing the FOV of the reconstructed holograms of the red channel (660 nm) than the green channel (520 nm). Specifically, the FOV for the red channel is scaled by a factor of 450 nm/660 nm and the FOV for the green channel is scaled by a factor of 520 nm/660 nm. For the monochromatic evaluation the full FOV of the red channel (660 nm) is used.

**Table S1:** Quantitative evaluation of 64× and 16× étendue expansion reconstructions. All reconstructions are evaluated after frequency filtering. Error bars correspond to one standard deviation. The highest performing score for each setting is highlighted in **bold**.

	Neural Étendue Expander	Uniform Random Expander	Binary Random Expander <sup>1</sup>	Photon Sieves <sup>3</sup>
64× Monochromatic 660 nm	<b>29.1 ± 2.3</b>	17.4 ± 1.6	17.4 ± 1.6	13.5 ± 1.1
64× Trichromatic All Colors	<b>31.6 ± 3.6</b>	16.8 ± 1.5	13.6 ± 1.2	13.1 ± 1.0
64× Trichromatic 660 nm	<b>39.9 ± 8.4</b>	19.9 ± 2.9	19.8 ± 2.9	13.0 ± 1.5
64× Trichromatic 520 nm	<b>33.4 ± 4.2</b>	16.0 ± 1.6	11.9 ± 0.9	13.4 ± 1.1
64× Trichromatic 450 nm	<b>21.6 ± 4.4</b>	14.6 ± 2.2	9.2 ± 1.7	12.8 ± 1.8
16× Monochromatic 660 nm	<b>49.7 ± 4.0</b>	25.6 ± 3.8	25.5 ± 3.8	13.5 ± 1.0
16× Trichromatic All Colors	<b>47.4 ± 4.2</b>	31.9 ± 5.0	24.2 ± 3.4	13.2 ± 1.0
16× Trichromatic 660 nm	<b>54.8 ± 2.9</b>	47.3 ± 9.6	46.8 ± 9.9	13.3 ± 1.4
16× Trichromatic 520 nm	<b>51.9 ± 4.0</b>	27.8 ± 6.3	16.1 ± 1.8	13.5 ± 1.1
16× Trichromatic 450 nm	<b>35.6 ± 9.2</b>	20.6 ± 4.3	9.8 ± 1.7	12.8 ± 1.8

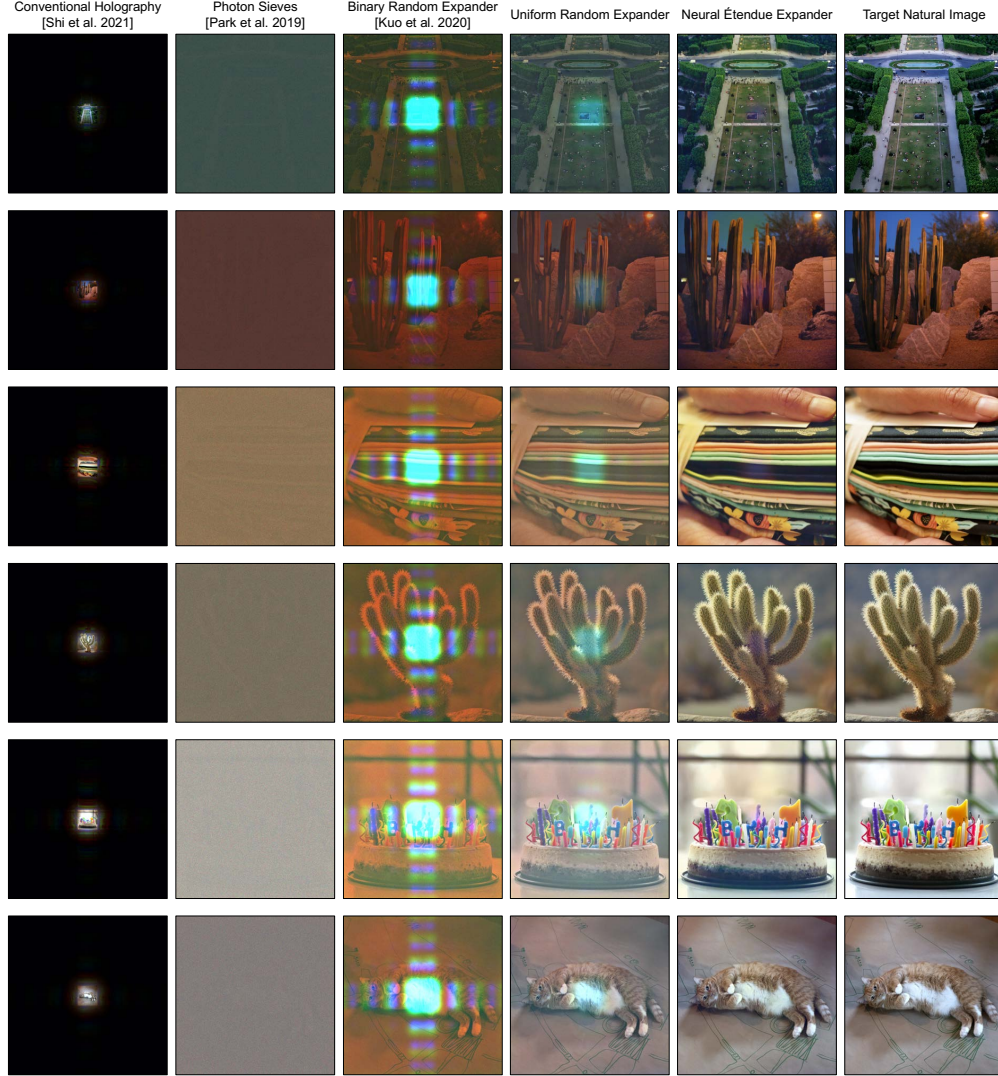


**Figure S7:** Simulated color holograms at  $64\times$  étendue expansion. The wavelengths used are 660 nm, 517 nm, and 450 nm. These experimental findings supplement the simulation results from Fig. 3 of the main manuscript.



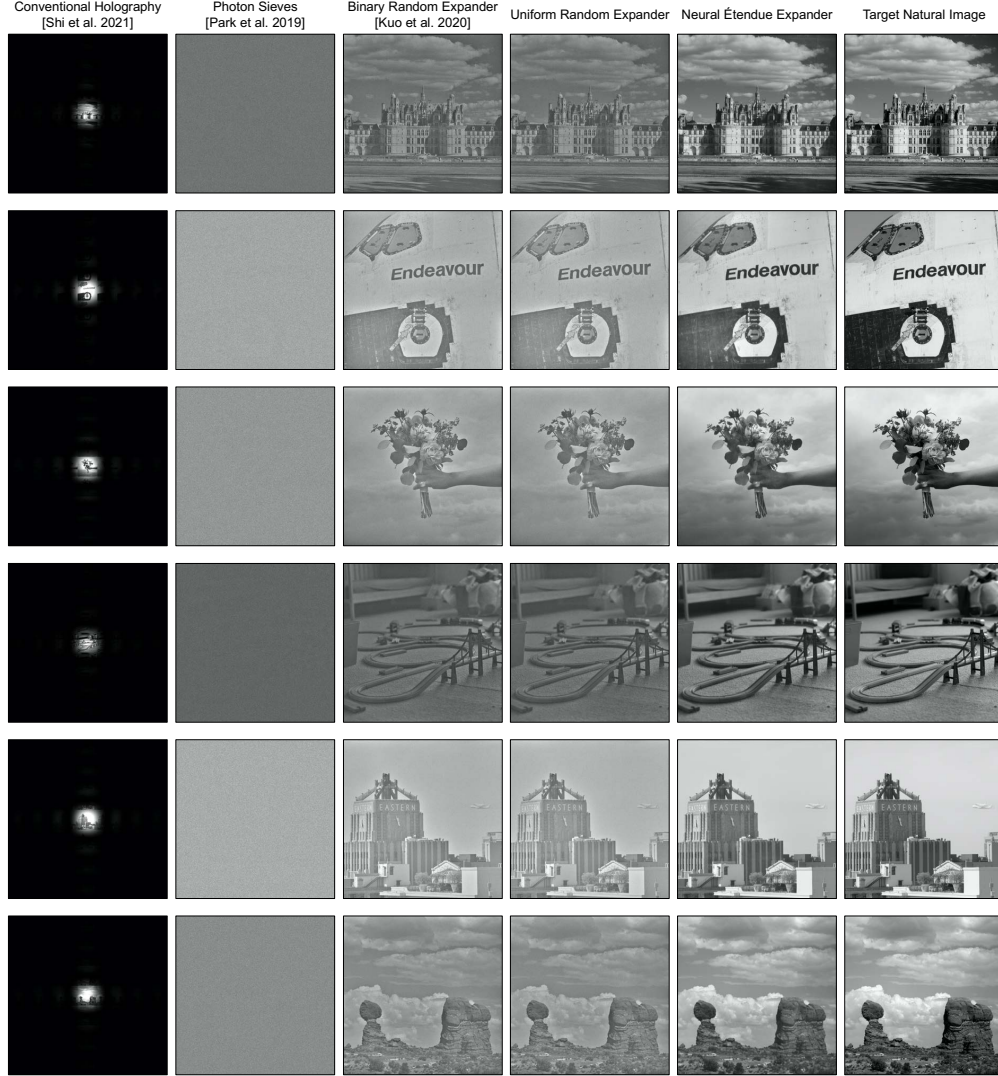


**Figure S8:** Simulated monochromatic holograms at  $64\times$  étendue expansion. The wavelength used is 660 nm. These experiments supplement the simulation results from Fig. 3 of the main manuscript.

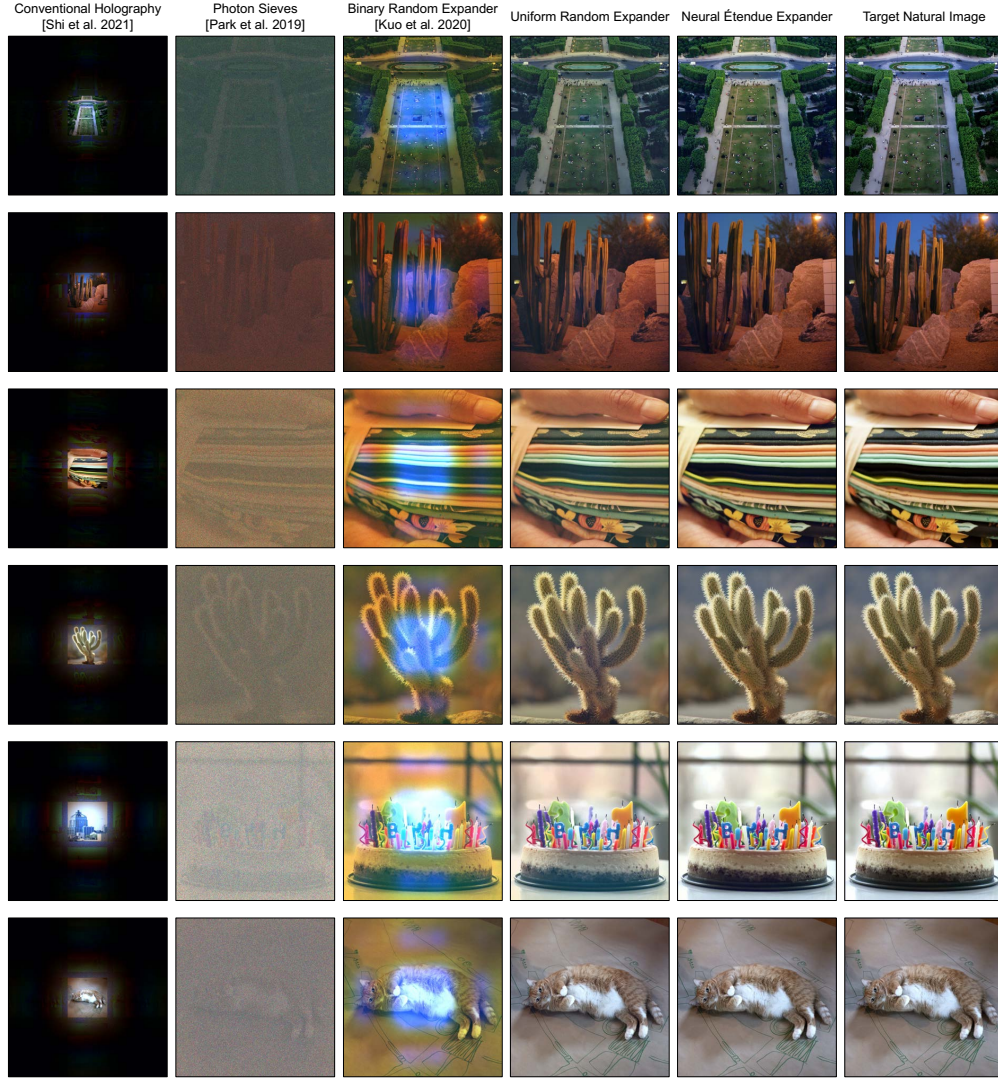


**Figure S9:** Simulated color holograms at  $16\times$  étendue expansion. The wavelengths used are 660 nm, 517 nm, and 450 nm. These experiments supplement the simulation results from Fig. 3 of the main manuscript.



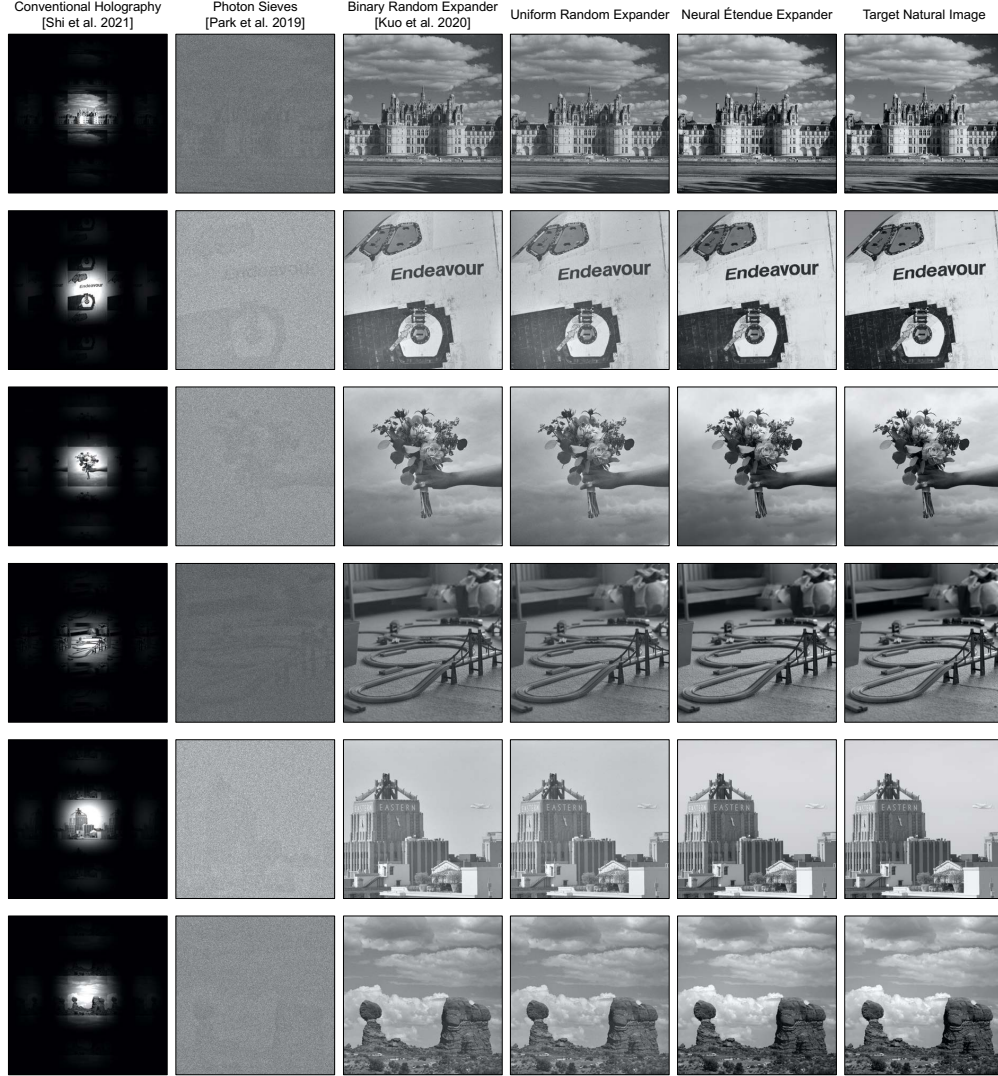


**Figure S10:** Simulated monochromatic holograms at  $16\times$  étendue expansion. The wavelength used is 660 nm. These experiments supplement the simulation results from Fig. 3 of the main manuscript.

### Supplementary Note 3: Expander Analysis

In this section we provide additional analysis and derivations of the virtual frequency upper bound and the display specifications when our method is integrated with an 8K SLM<sup>8</sup>.

**Derivation of Virtual Frequency Upper Bound** Here we provide further steps to show how we obtained the upper bound described by Equation 2 in the main manuscript.

$$\begin{aligned}
\mathcal{L}_T &= \min_{\mathcal{S}} \left\| (|\mathcal{F}(\mathcal{E} \odot U(\mathcal{S}))|^2 - T) * f \right\|_2^2 \\
&\leq \left\| (|\mathcal{F}(\mathcal{E})|^2 - T) * f \right\|_2^2 \\
&= \frac{1}{N} \left\| (\mathcal{F}(|\mathcal{F}(\mathcal{E})|^2) - \mathcal{F}(T)) \odot \mathcal{F}(f) \right\|_2^2 \\
&= \frac{1}{N} \left\| (\tilde{\mathcal{E}} - \mathcal{F}(T)) \odot \mathcal{F}(f) \right\|_2^2.
\end{aligned} \tag{S1}$$

The inequality is obtained because the loss value that is obtained with the optimum setting for  $\mathcal{S}$  must be less than or equal to the loss value when  $\mathcal{S}$  is uses the zero-phase setting. This upper bound manifests itself in the learned frequency spectrum of the neural étendue expanders. See Supplementary Fig. S11 for a comparison between the virtual frequency modulation of the learned neural étendue expanders and the virtual frequency modulation of natural images.

**Étendue-expanded Display Specifications** Here we provide the derivation of the FOV and eyebox sizes after étendue expansion. We first assume an 8K SLM<sup>8</sup> with  $7680 \times 4320$  pixel resolution at 660 nm wavelength. We augment the SLM with a  $64\times$  étendue expander, resulting in  $61440 \times 34560$  pixel resolution. Now the FOV and eyebox size are related to each other by

$$\text{FOV} \times \text{eyebox} = \lambda \times N_n, \tag{S2}$$

where  $N_n$  is the expanded pixel resolution<sup>1</sup>. By setting the eyebox to 18.5 mm we get a horizontal FOV of  $126^\circ$  and a vertical FOV of  $71^\circ$ . The stereo FOV provided is given by

$$\text{Stereo FOV} = 4 \arcsin(\sin(\text{Horizontal FOV}/2) \times \sin(\text{Vertical FOV}/2)). \tag{S3}$$

Thus, the total stereo FOV provided is 2.175 steradians. Human stereo FOV is 2.56 steradians<sup>9</sup> so this étendue expanded holographic display would provide a stereo FOV that covers 85% of the human stereo FOV. Note that this value could vary per individual.

For this same system, the provided angular resolution is given by

$$\text{Angular Resolution} = N_s / \text{FOV} \tag{S4}$$

where  $N_s$  is the native SLM resolution. Thus, the angular resolution is 61 pixels/degree for the setup assumed above.

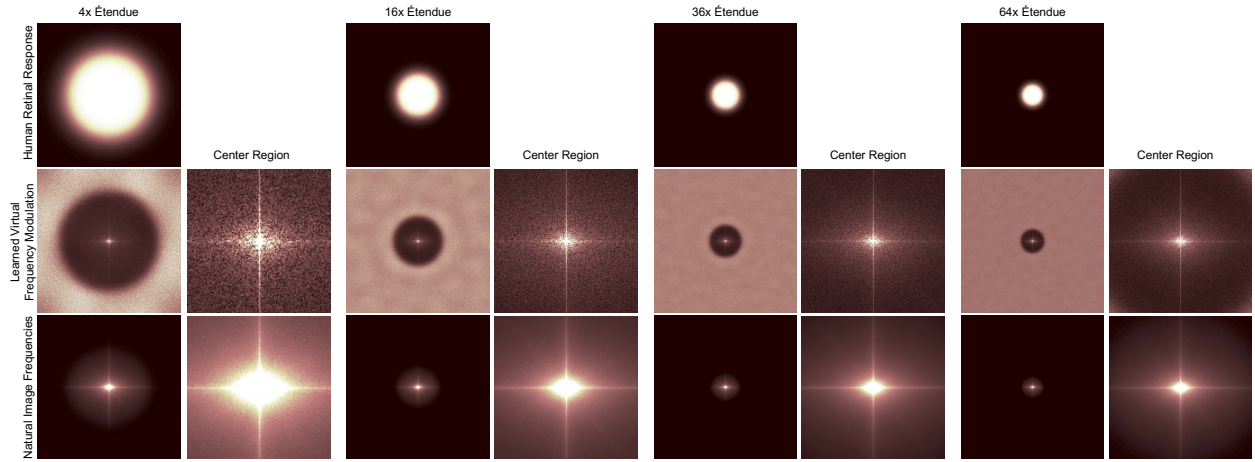


**Figure S11:** Comparison of virtual frequency modulation of neural étendue expander and natural images. Most content for natural images resides within the lower frequency bands. The human visual system is also largely biased towards the lower frequency terms. We coarsely approximate the human visual response with low pass filters (top row). Our training algorithm teaches the expander to learn a virtual frequency modulation (middle row) that approximates the frequency modulation of a natural image dataset (bottom row). The center region insets correspond to the center eighth of each spectrum.

#### Supplementary Note 4: Étendue Expansion for 3D Holograms

Neural étendue expanders also facilitate the generation of 3D holograms. To demonstrate this, we optimize the SLM to produce 3D focal stack holograms. Specifically, we solve a variant of Eq. (3) from the main manuscript. This variant is given by

$$\underset{\mathcal{E}, \mathcal{S}}{\text{minimize}} \left\| (|\mathcal{F}(\mathcal{E} \odot U(\mathcal{S}))|^2 - T_{\text{near}}) * f \right\|_2^2 + \left\| (|\mathcal{F}(\mathcal{Z} \odot \mathcal{E} \odot U(\mathcal{S}))|^2 - T_{\text{far}}) * f \right\|_2^2, \quad (\text{S5})$$

where  $T_{\text{near}}$  is the target image at the near plane,  $T_{\text{far}}$  is the target image at the far plane, and  $\mathcal{Z}$  is a z-offset phase given by

$$\mathcal{Z}(x, y) = \frac{2\pi}{\lambda} \frac{(x^2 + y^2)}{2f} \quad (\text{S6})$$

where  $f$  is the z-distance of the defocus and  $\lambda$  is the wavelength of the laser source. Within the HOLOEYE software the distance  $f$  can be set with a slider  $s$  as

$$f = \frac{\max(h, w) \cdot \Delta_{\text{SLM}}}{\lambda \cdot s} \quad (\text{S7})$$

where  $h$  is the height of the SLM,  $w$  is the width of the SLM, and  $\Delta_{\text{SLM}}$  is the SLM pixel pitch. Solving Equation S5 will produce a two plane étendue expanded 3D hologram. Simulated qualitative results are shown in Supplementary Fig. S12. We used  $s = -0.005$  for these results. The physical separation of the two focal planes also depends on the focal length of the Fourier Transforming lens. For the 80 mm lens used in our setup this setting of  $s$  results in a physical separation of approximately 3 mm.

Neural étendue expansion achieves high-fidelity étendue expanded 3D color holograms. We measure over 5 dB improvement in PSNR over 3D color holograms generated with uniform random expanders. We note that no existing étendue expansion technique has successfully demonstrated 3D color holography aside from photon sieves. However, the photon sieve expansion method only supports 3D holography of sparse points and not natural scenes.

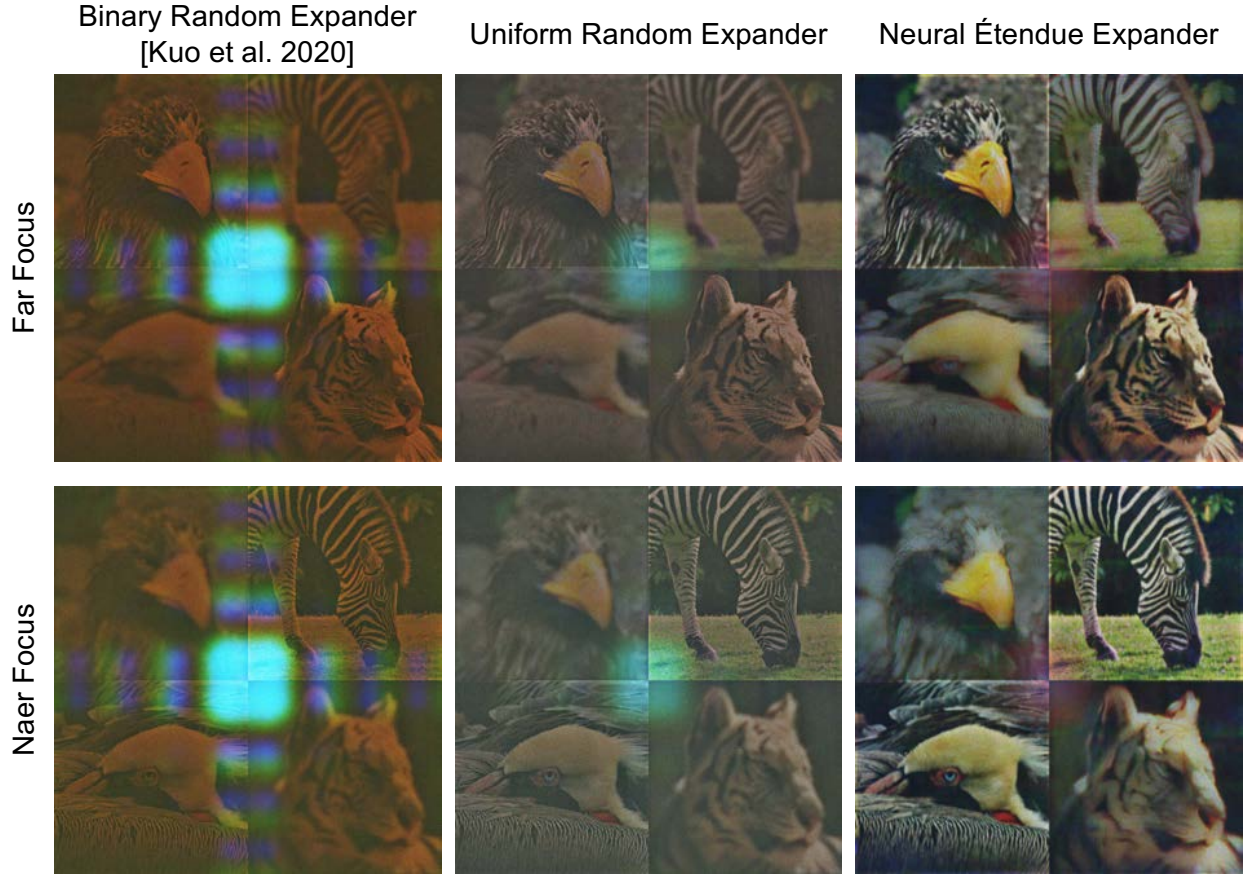


**Figure S12:** Simulated results for étendue expanded 3D color holograms. Here we show trichromatic holograms generated at 660 nm, 517 nm, and 450 nm at two different depth planes. The near plane corresponds to 0 mm and the far plane corresponds to a separation of 3 mm when using an 80 mm focal length lens as the Fourier Transforming lens. Similar to the étendue expanded 2D hologram results, neural étendue expanders are capable of improving the fidelity of étendue expanded 3D holograms of natural scenes. In contrast, the uniform and binary random expanders achieve lower fidelity.

## Supplementary Note 5: Eyebox Analysis

In this section we evaluate the robustness of different étendue expansion methods to changes in the eye pupil position and size. We vary the eye pupil setting and we apply pupil-aware holography<sup>7</sup> to the holograms generated with binary random expanders<sup>1</sup>, quadratic phase profiles<sup>10</sup>, and neural étendue expanders. Quantitative performance is shown in Supplementary Table S2 and qualitative results are shown in Supplementary Figures S13 and S14.

We observe that neural étendue expanders supports high-fidelity holograms varying pupil positions and sizes. This is because we initialized the learning process with a random expander which biases the final solution towards solutions that spread energy evenly throughout the eyebox. Quadratic phase profiles do not truly expand étendue, they increase the FOV but change the energy distribution within the eyebox. Hence, changing the eye pupil setting causes image content to disappear, even when combined with pupil-aware holography.



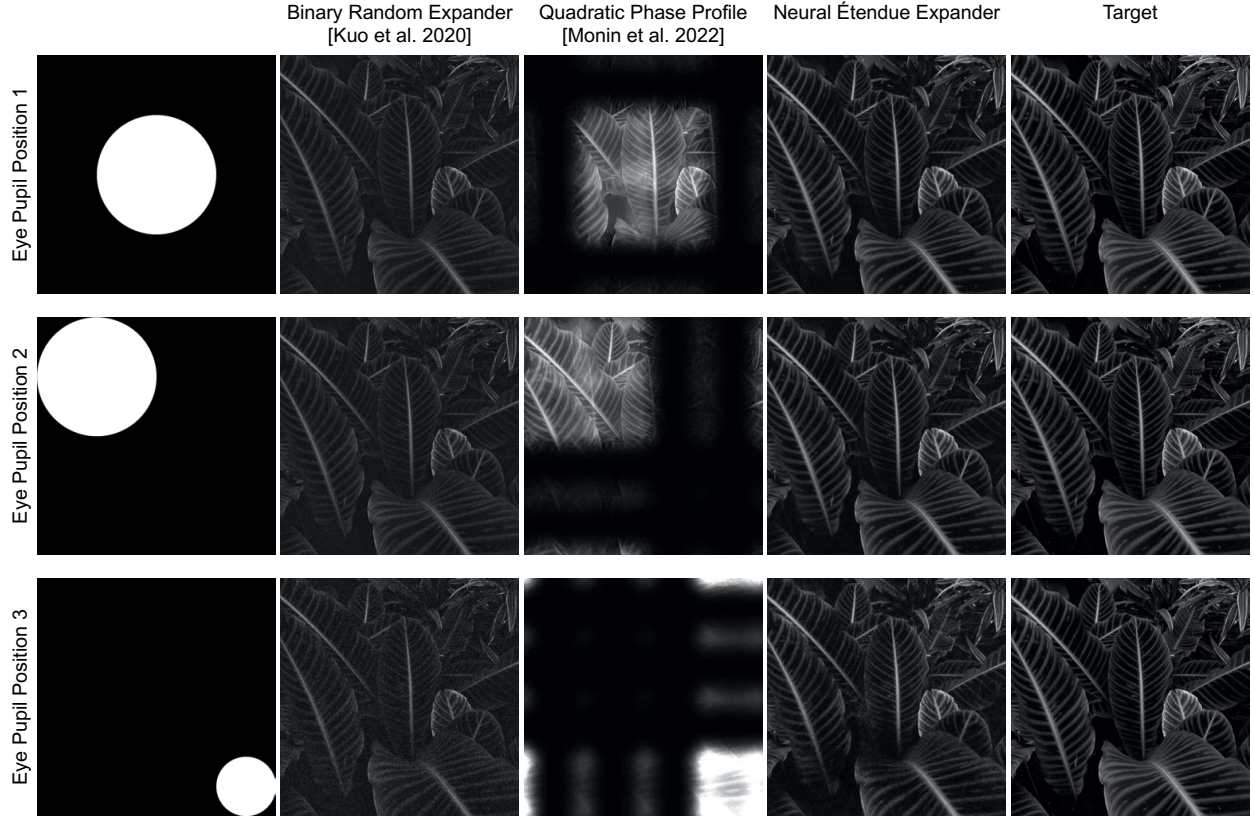


**Figure S13:** Impact of eye pupil movement on perceived hologram. The eye pupil position and size is shown in the left column. The reconstructed étendue expanded holograms are shown for binary random expanders<sup>1</sup>, quadratic phase profiles<sup>10</sup>, and neural étendue expanders. Changes in the eye pupil position causes image content to disappear when using quadratic phase profiles. Neural étendue expansion and random expansion both support a complete eyebox where the position of the eye pupil does not significantly affect the perceived image content. Furthermore, neural étendue expansion outperforms random expansion at all eye pupil positions. These holograms are simulated at  $16\times$  étendue expansion.

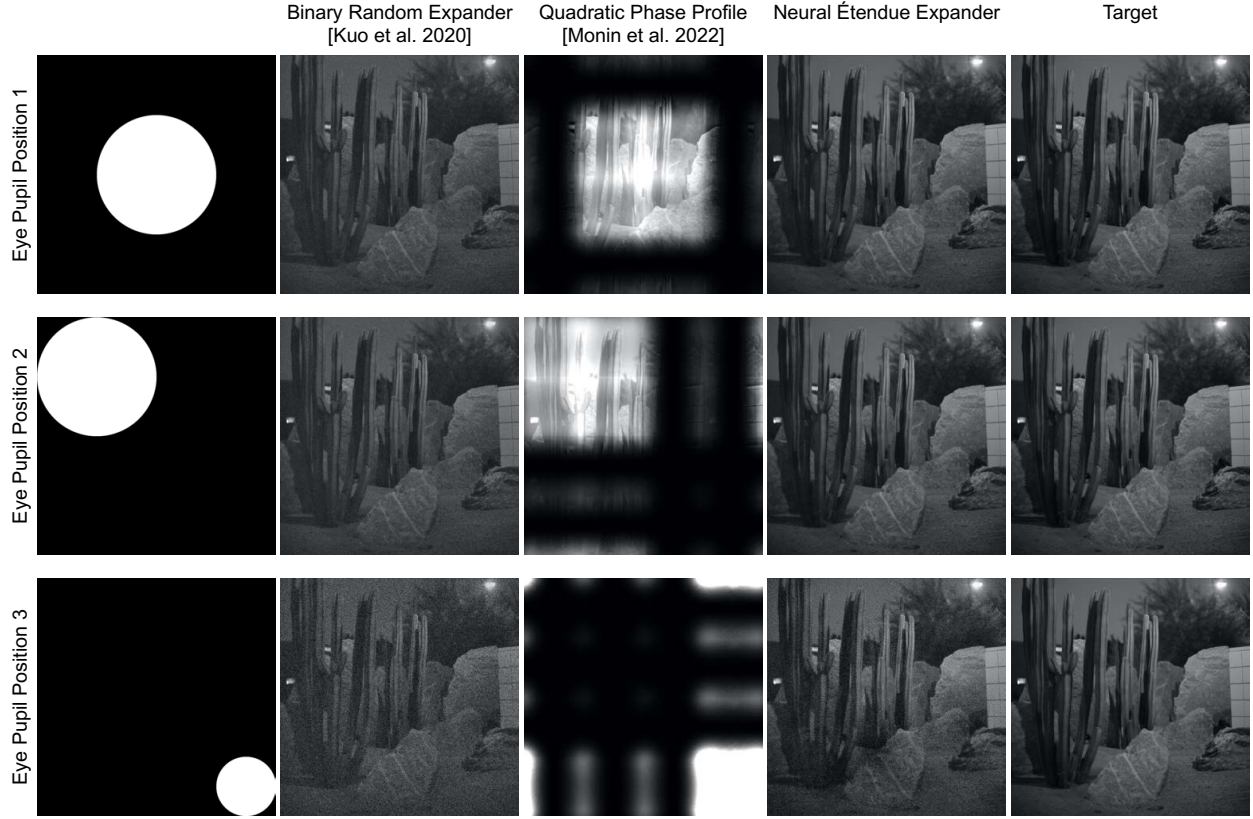


**Figure S14:** Impact of eye pupil movement on perceived hologram. The eye pupil position and size is shown in the left column. The reconstructed étendue expanded holograms are shown for binary random expanders<sup>1</sup>, quadratic phase profiles<sup>10</sup>, and neural étendue expanders. Changes in the eye pupil position causes image content to disappear when using quadratic phase profiles. Neural étendue expansion and random expansion both support a complete eyebox where the position of the eye pupil does not significantly affect the perceived image content. Furthermore, neural étendue expansion outperforms random expansion at all eye pupil positions. These holograms are simulated at  $16\times$  étendue expansion.



**Table S2:** Quantitative evaluation of  $16\times$  étendue expansion reconstructions with different eye pupil positions. All reconstructions are evaluated after frequency filtering. Error bars correspond to one standard deviation. The highest performing score for each eye pupil setting is highlighted in **bold**.

	Neural Étendue Expander	Quadratic Phase Profile <sup>10</sup>	Binary Random Expander <sup>1</sup>
Eye Pupil Position 1	<b><math>24.5 \pm 4.4</math></b>	$7.3 \pm 2.3$	$18.7 \pm 3.5$
Eye Pupil Position 2	<b><math>24.7 \pm 4.6</math></b>	$7.9 \pm 2.5$	$18.7 \pm 3.5$
Eye Pupil Position 3	<b><math>17.7 \pm 2.7</math></b>	$7.1 \pm 1.7$	$15.5 \pm 2.4$

## Supplementary Note 6: Resolution Analysis

In this section we simulate étendue expansion with different native SLM resolutions from 1K-pixels to 8K-pixels. The results are reported in Supplementary Table S3. We observe negligible changes in reconstruction fidelity across different SLM resolutions. This validates that the reconstruction fidelity depends only on the étendue expansion factor and not on the pixel resolution. Furthermore, this means that our technique when combined with an 8K SLM could provide the necessary stereo FOV and eyebox size needed for an immersive AR/VR experience, as per the specifications discussed in Supplementary Note 3.

While the perceived display quality of a practical system depends on many factors such as the SLM’s pixel fill factor and the expander’s diffraction efficiency, these are factors separate from the analysis that we are performing. Here, we assume ideal devices and hardware construction to demonstrate that the theoretical improvement in reconstruction fidelity for a given étendue expansion factor does not change for different native SLM resolutions. Compensating for non-idealities in practical hardware can be accomplished with recent developments in neural holography<sup>2,3</sup>.

**Table S3:** Quantitative evaluation of  $64\times$  étendue expansion reconstructions for different native SLM resolutions. All reconstructions are evaluated after frequency filtering. Error bars correspond to one standard deviation. The highest performing score for each setting is highlighted in **bold**.

Native SLM Resolution	Neural Étendue Expander	Uniform Random Expander	Binary Random Expander <sup>1</sup>
1K	<b><math>29.1 \pm 2.3</math></b>	$17.4 \pm 1.6$	$17.4 \pm 1.6$
2K	<b><math>29.1 \pm 2.3</math></b>	$17.4 \pm 1.6$	$17.4 \pm 1.5$
4K	<b><math>29.0 \pm 2.2</math></b>	$17.5 \pm 1.5$	$17.4 \pm 1.6$
8K	<b><math>29.0 \pm 2.2</math></b>	$17.4 \pm 1.5$	$17.4 \pm 1.6$

## **Supplementary Note 7: Étendue Expansion with Higher Order Filtering**

The étendue expanded holograms are formed as the convolution of the far field wavefronts of the expander and the SLM<sup>1</sup>. Both of these far fields contain repeated copies or echoes as shown in Supplementary Figure S15. When these far fields are convolved the echoes are intertwined, resulting in undesirable copies within the étendue expanded hologram.

These copies do not noticeably degrade the quality of holograms of natural images. Nevertheless, if these copies must be removed then it can be performed by placing an amplitude block at the same location within the 4F system as the DC block. The amplitude block filters the higher order echoes coming from the SLM, as shown in Supplementary Figure S15. Simulated étendue expanded holograms with this block are shown in Supplementary Figure S16 and demonstrate that the undesired copies are removed.

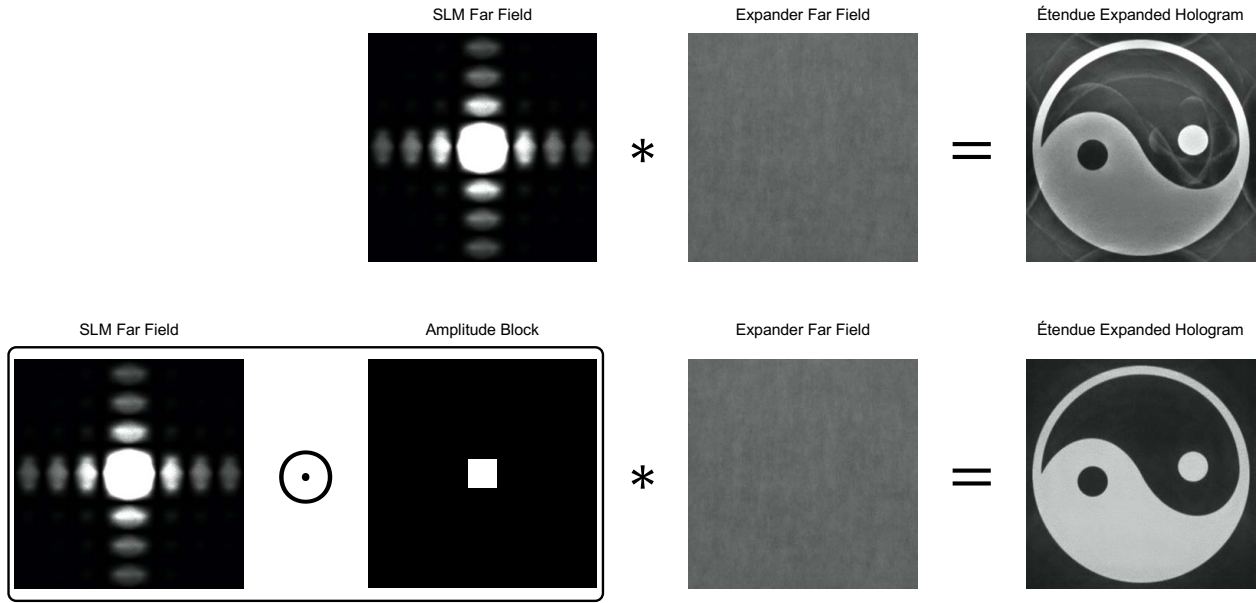


**Figure S15:** Removing undesired copies within étendue expanded holograms. Étendue expanded holograms contain undesirable copies because the SLM's far field wavefront contains higher order echoes. Placing a square amplitude block within the 4F system will remove the SLM's higher order echoes. This in turn removes the undesirable copies within the étendue expanded hologram.

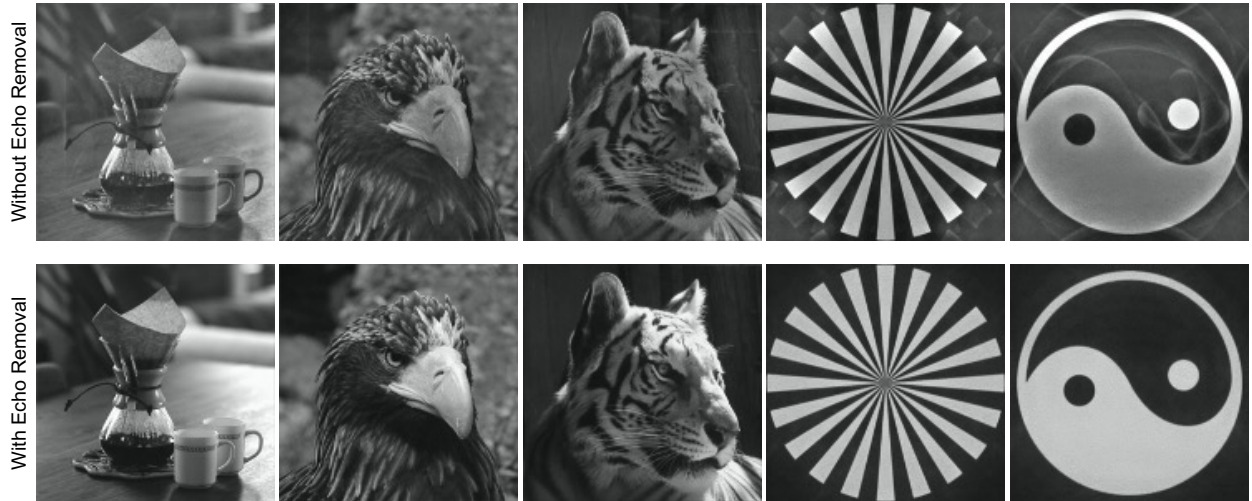


**Figure S16:** Simulated results for étendue expanded holograms with and without higher order echo filtering, see text for detailed description.

## Supplementary Note 8: Expander Fabrication

The expanders are physically realized as diffractive optical elements (DOE). The laser writer used for etching the stamp is capable of producing 8 levels of quantization. We set the heights of the DOE to have full  $2\pi$  phase range modulation at 660 nm. Therefore, the 8 height levels of the DOE correspond to 0  $\mu\text{m}$ , 0.1624  $\mu\text{m}$ , 0.3247  $\mu\text{m}$ , 0.4871  $\mu\text{m}$ , 0.6495  $\mu\text{m}$ , 0.8118  $\mu\text{m}$ , 0.9742  $\mu\text{m}$ , and 1.1366  $\mu\text{m}$ . Note that this gives us greater than  $2\pi$  phase range for the other wavelengths.

The total mask area of the DOEs spans 8.192 mm  $\times$  8.192 mm. This same area stays constant across all étendue expansion factors. For  $16\times$  étendue expansion the size of each pixel on the DOE is 8  $\mu\text{m} \times 8 \mu\text{m}$ , corresponding to  $1024 \times 1024$  total pixels. For  $64\times$  étendue expansion the size of each pixel on the DOE is 4  $\mu\text{m} \times 4 \mu\text{m}$ , corresponding to  $2048 \times 2048$  total pixels.

Microscope images of the fabricated DOEs corresponding to the optimized neural étendue expanders are shown in Fig. S17. Microscope images of the fabricated DOEs corresponding to the random patterns are shown in Fig. S18. Pictures of the DOEs are shown in Fig. S19. These images were captured on a Leica DCM 3D confocal microscope.

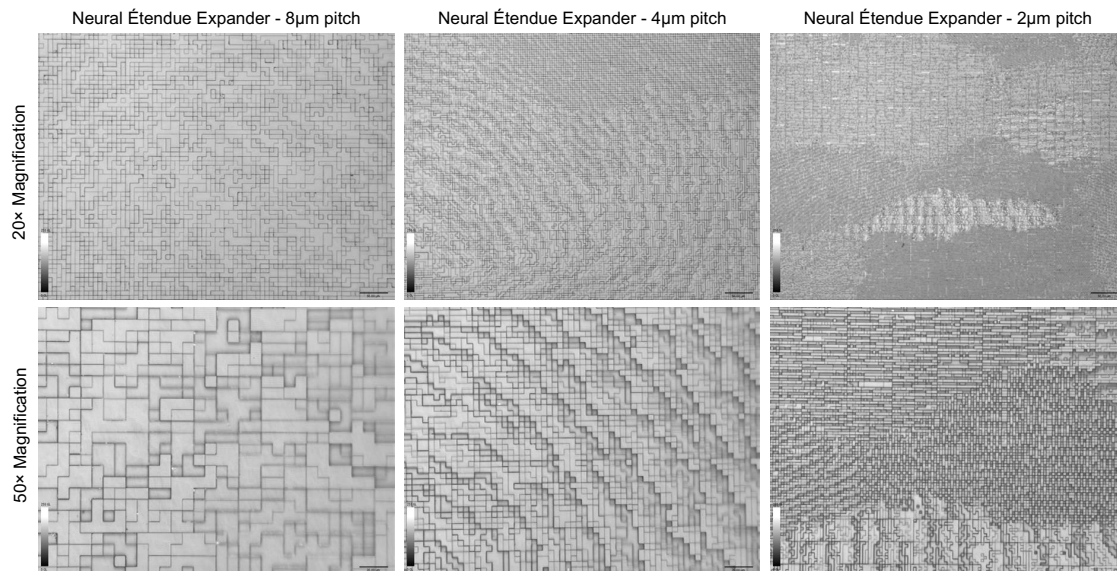


**Figure S17:** Confocal microscope imaging of neural étendue expander DOEs. These images are recorded at 20 $\times$  and 50 $\times$  magnification. Note that these DOEs fully utilize the 8 level quantization which results in several different height levels in these DOEs. Scale bars are shown on the bottom right.

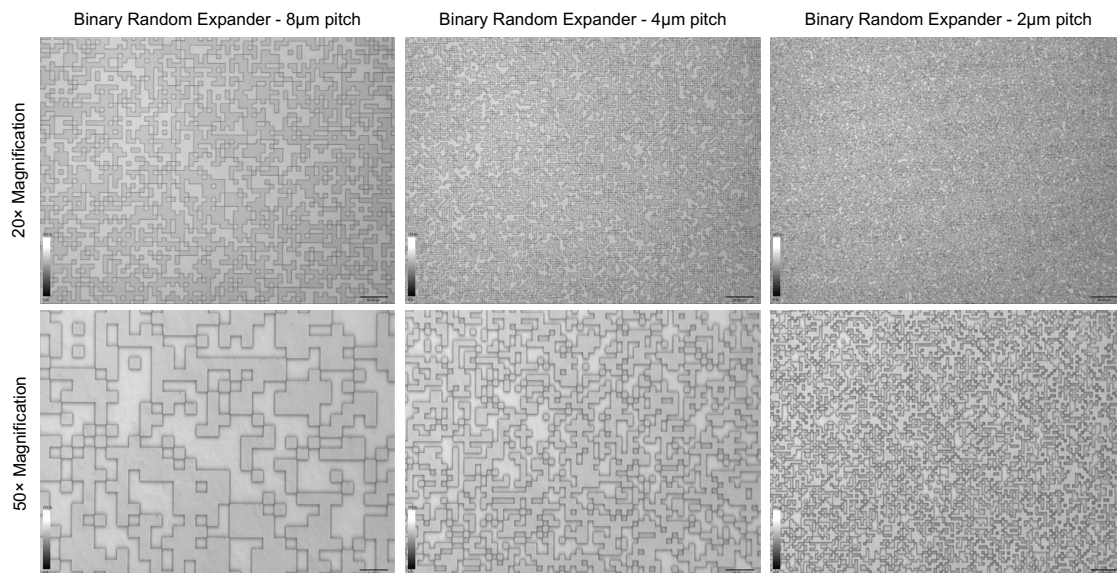


**Figure S18:** Confocal microscope imaging of random expander DOEs. These images are recorded at 20 $\times$  and 50 $\times$  magnification. Note that these DOEs only consist of 2 levels, 0  $\mu\text{m}$  and 0.6495  $\mu\text{m}$ . Scale bars are shown on the bottom right.

Picture of Spatial Light Modulator



Picture of Fabricated Neural Étendue Expanders

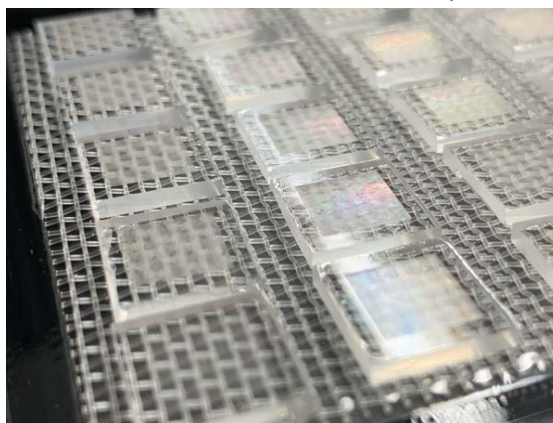


**Figure S19:** Photographs of the fabricated DOEs. This picture shows the stamped resin on top of the glass substrate. A picture of the SLM is shown for comparison.



## Supplementary Note 9: Experimental Setup

We built an experimental setup to validate the neural étendue expanders. The setup consists of two main components: the SLM and the expander.

The holograms are physically realized by illuminating the SLM with a coherent, collimated laser. A single Fourier transforming lens is placed after the expander in order to produce the Fourier holograms. Finally, we use a camera to take pictures of the holograms. A schematic of this setup is shown in Supplementary Figure S21 and a picture of the physical prototype is shown in Supplementary Figure S20. A full list of parts is shown in Supplementary Table S4. Note that our DC blocks are custom made by Frontrange Photomasks, a picture of the DC blocks are shown in Supplementary Figure S22.

The current prototype uses a 4F relay system to relay the SLM onto the expander which results in a bulky form factor. In the future a smaller form factor could be achieved by directly integrating the expander onto the SLM.

**Table S4:** Equipment list for building the experimental prototype.

Equipment	Product Name	Notes
Red Laser Diode	Thorlabs LP685-SF15	
Green Laser Diode	Thorlabs LP520-SF15	
Blue Laser Diode	Thorlabs LP450-SF15	
Laser Collimation Lens	Thorlabs AC254-200-A-ML	Used to collimate the laser source
Half Waveplate	Thorlabs CRM1-LTM	Used to adjust the polarization of the laser
Linear Polarizer	Thorlabs CRM1	Used to adjust the polarization of the laser
Beam Splitter	Thorlabs CCM1-4ER	
Spatial Light Modulator (SLM)	HOLOEYE PLUTO-2 SLM	
SLM Mount	Thorlabs PY005/M	Used to adjust the orientation of the SLM
4F System Lenses	Pentax SMC FA 75 mm $f/2.8$	Two of the same lenses are required
4F System Lens Mounts	Thorlabs PY005/M	Used to adjust the orientation of the lenses
DC Block	100 $\mu$ m chrome dot on glass	Used to filter out the SLM's DC term
DC Block Holder	Thorlabs KM100S	Used to filter out the SLM's DC term
5-axis translation stage	Thorlabs Nanomax 300	Used to adjust the position of the expander
Expander Holder	Thorlabs KM100C	Provides a 6th-axis for position adjustment
Fourier Transforming Lens	Thorlabs AC508-080-A-ML	Used to produce the Fourier hologram
Imaging Lens	Thorlabs AC508-100-A-ML	
Camera Lens	Computar C-Mount 25 mm Lens	
Camera	FLIR Blackfly S BFS-U3-200S6M	
Shear Interferometer	Thorlabs SI254	Used to build the system
Mirror	Thorlabs PF10-03-P01	Used to build the system
Pinhole	Thorlabs LMR1AP	Used to build the system

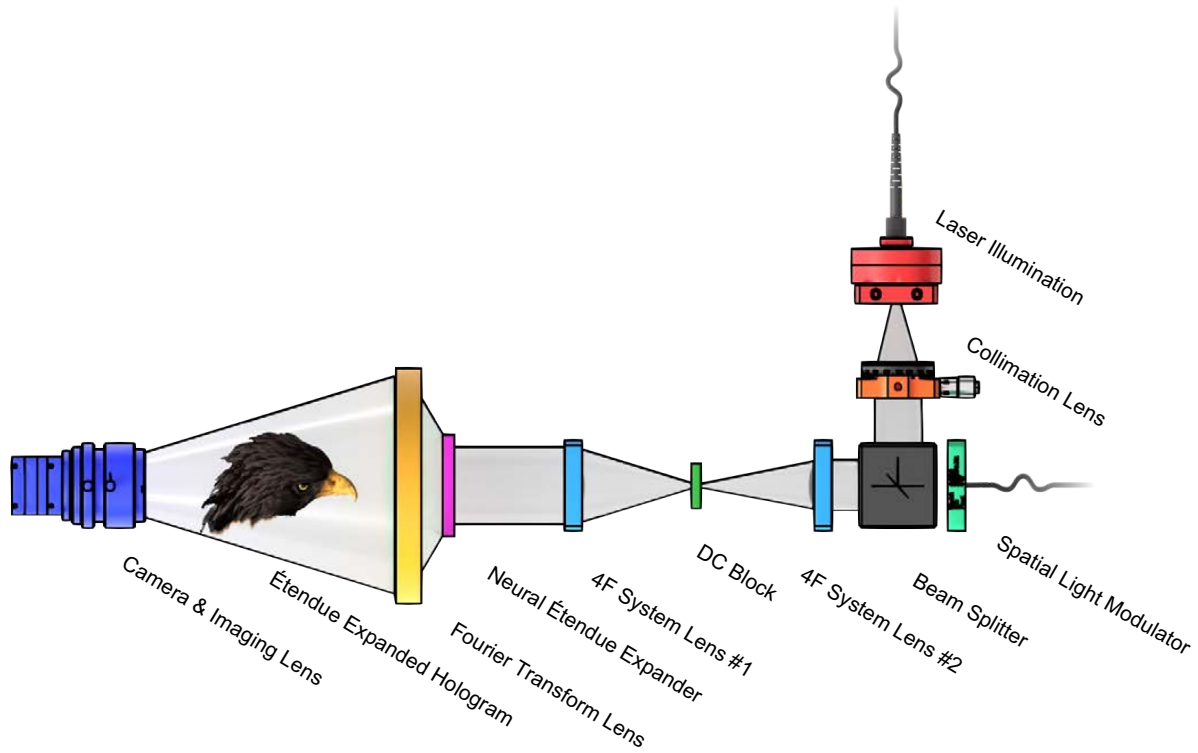


**Figure S20:** Schematic of experimental setup. Starting from the laser source, the collimating lens turns the laser source into a coherent, collimated beam. We use a half waveplate and a linear polarizer to adjust the polarization of the laser so that it matches the polarization of the SLM. The laser enters the beam splitter cube and the SLM reflects the laser light into the 4F system. The 4F system serves to filter out the SLM DC term via the DC block and also to relay the SLM onto the expander. Once the laser light passes through the expander it is then focused by the Fourier transforming lens to produce the Fourier hologram. This hologram is then imaged by the camera.

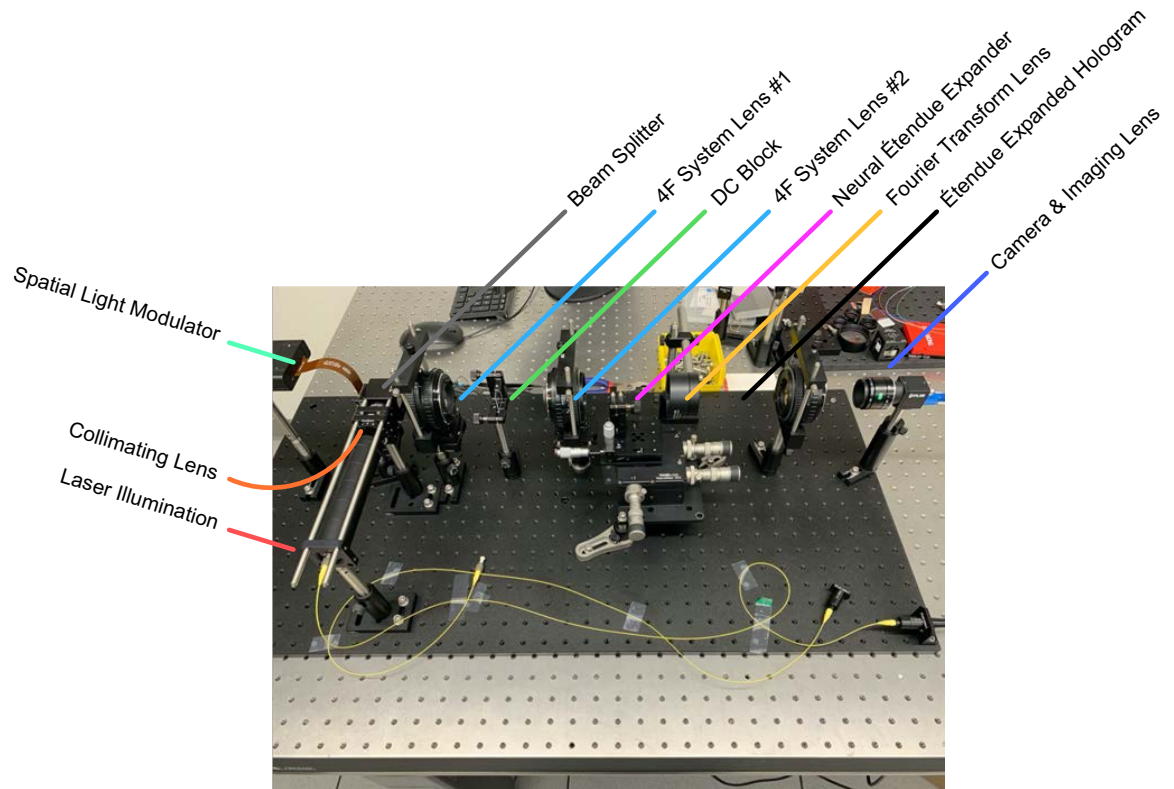


**Figure S21:** Picture of the physical prototype. We constructed this prototype using the parts described in Supplementary Table S4. The physical realization of each component described in Supplementary Figure S20 is labeled. The neural étendue expander is mounted within the translation mount pointed to by the label. The étendue expanded hologram is formed in the space after the Fourier Transforming lens. The hologram cannot be seen in this picture as it can only be seen from the position of the Camera & Imaging Lens.

Picture of DC Block



**Figure S22:** Picture of a DC block. We fill the center of a square piece of glass with a chrome filling. The chrome blocks out the undiffracted DC component of the SLM when placed at the Fourier plane of the 4F system. The diameter of the chrome filling shown in this picture is 1000  $\mu\text{m}$ . For the hardware prototype we used a DC block which has a chrome filling with a smaller diameter of 100  $\mu\text{m}$ .

## Supplementary Note 10: Hardware Prototype Construction

In this section, we detail the calibration and alignment procedures we use for the proposed setup.

**SLM Calibration** The voltage levels on the reflective SLM need to be calibrated for maximum performance. This is done via the HOLOEYE PLUTO-2 Configuration Manager. Within the configuration manager we set the voltage look-up table to maximize the optical power in the first order at the red wavelength (660 nm). The optical power was measured using a power meter (Thorlabs PM100). We also set the low level pixel voltage to 0.692 V and the high level pixel voltage to 1.286 V to produce a  $[0, 2\pi]$  phase range at 660 nm. Setting this phase range for the red wavelength allows for  $> 2\pi$  phase range for the green and blue wavelengths.

**4F System Alignment** We observed that the image quality significantly improves with better alignment. Hence, the following steps ensure that each element in the system is tightly bound and aligned to the main optical axis. Refer also to the equipment list in Table S4.

Set up the laser diode and the collimation lens. Use the shear interferometer to validate the collimation of the laser. Place the first 4F system lens after the beam splitter and the first pinhole. Ensure that the lens is mounted so that the optical axis is maintained through the other pinholes. This is done by looking at the laser dots formed on the other pinholes. If the alignment is off then a dot will be formed to the side of the pinhole. It is easiest to see these dots by affixing paper to the pinhole and working with the room lights off. Furthermore, it is also essential to inspect the dots formed via back reflections. Each lens is composed of several internal optical elements. If the alignment is off then internal reflections will occur within those elements and cause reflections back onto the first pinhole. Repeat for all other optical elements in the system. Note that this procedure must be conducted without the DC block in place.

**Polarization Calibration** Both the SLM and the laser diode are polarized. The maximum performance is achieved when the polarization states of the two elements are aligned. We will use a half-wave plate (HWP) to turn the polarization of the laser diode. We will use a linear polarizer (LP) after the HWP to eliminate stray polarization states. The goal of this stage is to align the HWP and the LP to the polarization state of the SLM. We used the following steps to align their polarization states.

First display the highest frequency blazed grating on the SLM. This pattern is designed by alternately setting each column of the SLM to be 0 or  $\pi$ . This pattern will produce a diffraction dot to the right of the main dot produced by the SLM's DC term. An echo of the diffraction dot also

will appear to the left of the main dot. We will use the right and left diffraction dots to determine the correct polarization. We turn the LP until the area of the diffracted dots is maximized. The size of the dot should change as you turn the LP. Ignore the setting of the HWP for now. No matter how the HWP is set, changing the LP will always change the size of the diffraction dot. Once the area of the diffracted dots is maximized, we now know that the LP corresponds to the SLM's polarization state, see Figure S23a. Now we turn the HWP until the intensity of the entire diffraction pattern is maximized, see Figure S23b. After doing this we know that the HWP and LP must be aligned to the SLM.

As one additional note, turning the LP by 90 deg from the correct setting without changing the HWP will create the pattern shown in Figure S23c. Observe how the area of the diffracted dots changes from Figure S23b but the main DC dot is mostly unaffected.

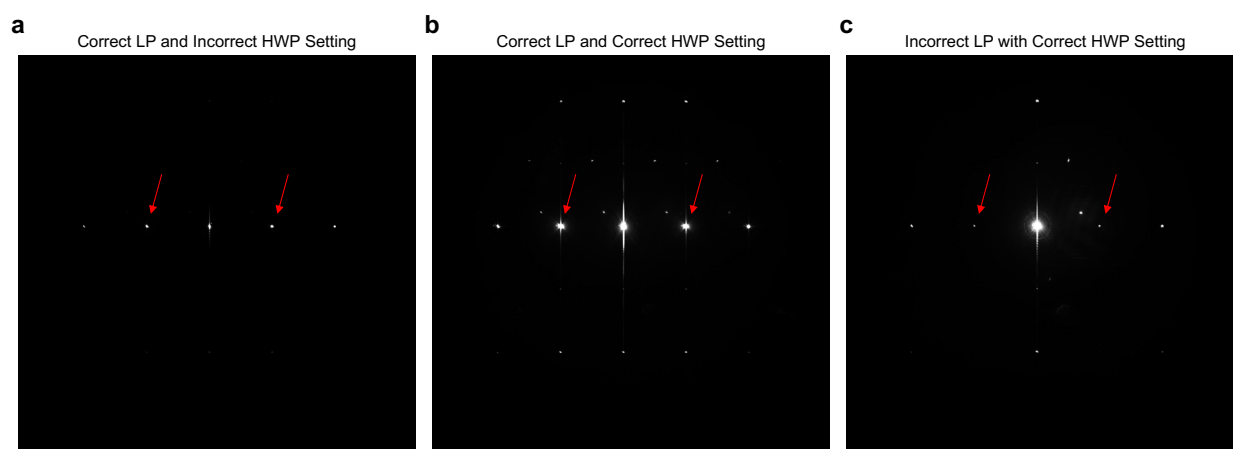


**Figure S23:** **a** Diffraction pattern when LP is set correctly while the HWP is set incorrectly. **b** Diffraction pattern when LP and HWP are set correctly. **c** Diffraction pattern when the LP is set incorrectly while the HWP is set correctly. Observe the size and intensity of the dots indicated by the red arrows.



**Expander Alignment Procedure** After the 4F system is constructed the expander needs to be placed at the precise location of the virtual SLM. This alignment step can be challenging because slight shifts in the expander position will result in a dramatic loss of contrast, oftentimes to the point where there is no discernible signal. Hence, the following steps are used to align the expander.

We construct a 6-axis adjustable translation and rotation stage by combining the Thorlabs KM100C with the Thorlabs Nanomax 300. This stage allows for micrometer-scale movement over the  $x, y, z$  axes and the roll, pitch, yaw axes. We mount the expander by placing it into the Thorlabs KM100C. We adjust the position of the expander until the illumination of the virtual SLM lies within the expander's boundaries.

We solve for an SLM pattern that will generate a hologram that contains a single dot. Do not use any binning on the SLM. We adjust the stage knobs until the dot is seen. Refer to Figure S24 for a capture of the dot. We then solve for an SLM pattern that will generate a hologram corresponding to a natural image. We display that SLM pattern on the SLM and we align the stage until the contrast of the hologram is maximized. Refer to Figure S25 for an example.

The reason that we begin with a dot hologram instead of going directly to a natural scene hologram is because the dot hologram is the most tolerant to alignment error. Therefore, even if the alignment is a little off the dot will be visible, whereas for natural scenes that will not be the case.

Note that the position of the relayed virtual SLM after the 4F system is slightly different for different wavelengths. Thus, the expander needs to be adjusted slightly for different colors for this version of the hardware prototype. Building a system that removes this wavelength variance is a next step.

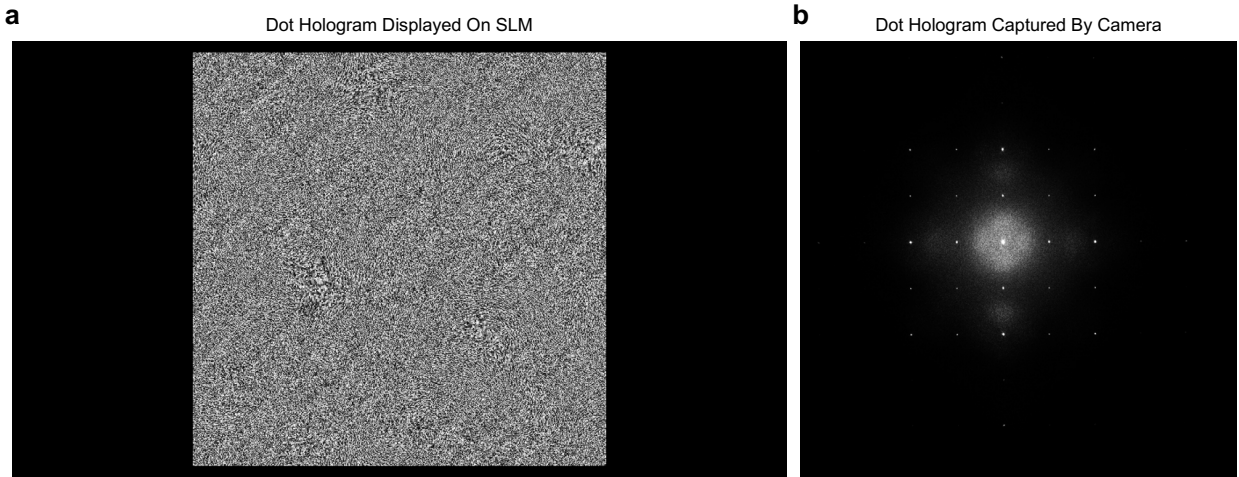


**Figure S24:** **a** SLM pattern that generates a single dot hologram produced through CGH. Display this pattern on the SLM when performing alignment. **b** Example of a dot hologram captured by the camera. Adjust the position of the expander until this dot hologram is shown. Note that the initial contrast of the dot may be low, further refinement of the alignment position is necessary to obtain higher contrast.

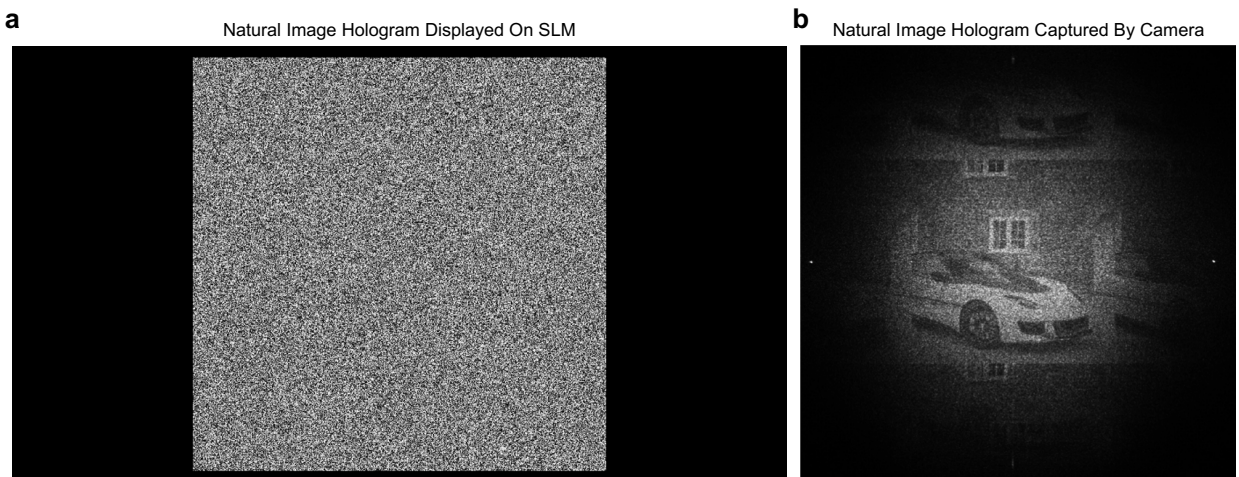


**Figure S25:** **a** SLM pattern that generates a natural image hologram produced through CGH. Display this pattern on the SLM when performing alignment. **b** Example of a natural image hologram captured by the camera. Note that the initial contrast may be low, further refinement of the alignment position is necessary to obtain higher contrast.

## References

1. Kuo, G., Waller, L., Ng, R. & Maimone, A. High resolution étendue expansion for holographic displays. *ACM Transactions on Graphics (TOG)* **39**, 1–14 (2020).
2. Shi, L., Li, B., Kim, C., Kellnhofer, P. & Matusik, W. Towards real-time photorealistic 3d holography with deep neural networks. *Nature* **591**, 234–239 (2021).
3. Park, J., Lee, K. & Park, Y. Ultrathin wide-angle large-area digital 3d holographic display using a non-periodic photon sieve. *Nature Communications* **10**, 1304 (2019).
4. Agustsson, E. & Timofte, R. Ntire 2017 challenge on single image super-resolution: Dataset and study. In *The IEEE Conference on Computer Vision and Pattern Recognition (CVPR) Workshops* (2017).
5. Jégou, H., Douze, M. & Schmid, C. Hamming embedding and weak geometric consistency for large scale image search. In *Proc. European Conference on Computer Vision (ECCV)* (2008).
6. Chakravarthula, P., Peng, Y., Kollin, J., Fuchs, H. & Heide, F. Wirtinger holography for near-eye displays. *ACM Transactions on Graphics (TOG)* **38**, 1–13 (2019).
7. Wyrowski, F. & Bryngdahl, O. Iterative fourier-transform algorithm applied to computer holography. *J. Opt. Soc. Am. A* **5**, 1058–1065 (1988).
8. Buckley, E., Cable, A., Lawrence, N. & Wilkinson, T. Viewing angle enhancement for two- and three-dimensional holographic displays with random superresolution phase masks. *Applied Optics* **45**, 7334–7341 (2006).
9. NASA, N. Space flight human-system standard volume 2: Human factors, habitability, and environmental health. Tech. Rep., NASA-STD-3001 (2011).
10. Monin, S., Sankaranarayanan, A. C. & Levin, A. Analyzing phase masks for wide étendue holographic displays. In *2022 IEEE International Conference on Computational Photography (ICCP)*, 1–12 (2022).